Device Nanofabrication and Quantum Electronic Trasnsport in Twisted van der Waals Heterostructures

by

Oriol Rubies Bigordà

Bachelor's Degree in Engineering Physics

and

Bachelor's Degree in Industrial Technology Engineering

MASSACHUSETTS INSTITUTE OF TECHNOLOGY

and

UNIVERSITAT POLITECNICA DE CATALUNYA

May 2019

Advisor .....

Prof. Pablo Jarillo-Herrero

Co-Advisor .....

Prof. Ramon Alcubilla

Abstract

The recent discovery of unconventional superconductivity and correlated insulating states in magic angle twisted bilayer graphene has gained the interest of the scientific community. This pioneering work has paved the way to a completely new field, twistronics, where flat bands are engineered to induce strongly correlated physics in twisted van der Waals heterostructures.

This thesis investigates the physics of two different Moiré systems. First, we report on a new platform to study correlated physics based on twisted bilayer-bilayer graphene, which consists of two sheets of AB bilayer graphene rotated by a small twist angle. We observe correlated insulating states for all integer electron fillings of the Moiré unit cell, which appear only in a finite range of electric displacement fields. The magnetic field dependence of the correlated insulators suggests the presence of magnetism in the system and differs significantly from the behavior found in magic angle twisted bilayer graphene. Additionally, we identify a strange metallic phase in magic angle twisted bilayer graphene for a range of fillings near the correlated insulators. The fabrication procedure to obtain twisted graphene structures is also discussed extensively.

Keywords: Condensed matter, Solid-state physics, Two-dimensional materials, Van der Waals heterostructures, Graphene, Twistronics, Magic angle graphene, Twisted bilayer graphene, Moire superlattices, Twisted bilayer-bilayer graphene, Strongly correlated physics, Strange metals, Planckian dissipation.

Acknowledgments

First of all, I am immensely grateful to Prof. Pablo Jarillo-Herrero, who gave me the opportunity to join this group and do high level research from the very first moment I stepped into the lab.

Also, I would like to thank the whole research group that has hosted me for the last 10 months. In particular, thanks to Daniel, Yuan and Jeong Min, with whom I have spent most of the time and from whom I have learned an immense amount of things.

I would also like to thank the Interdisciplinary Higher Education Center (CFIS) for making this great opportunity possible. My stay at MIT has also been feasible thanks to the financial support received from Fundació Privada Cellex.

Thanks also to all my friends at UPC, with whom I have enjoyed the last five years of undergraduate studies. A special mention for the people I have met in Boston: thanks to my Cambridge family (Jose, Martí, Mik and Núria) for the infinite adventures and travels all around the US; thanks to TSAPRR for the basketball games and their great company; and thanks to Manon for the wonderful moments shared during these months.

Most importantly, I want to express my most sincere gratitude to my parents Montse and Carlos and my sister Núria, for providing infinite support and advise during my whole life. Last, but not least, thanks to my grandparents for their guidance and lovely letters.

List of original publications

1. Yuan Cao, Debanjan Chowdhury, Daniel Rodan-Legrain, Oriol Rubies-Bigorda, Kenji Watanabe, Takashi Taniguchi, T. Senthil, Pablo Jarillo-Herrero. Strange metal in magic-angle graphene with near Planckian dissipation, arXiv:1901.03710

2. Yuan Cao, Daniel Rodan-Legrain, Oriol Rubies-Bigorda, Jeong Min Park, Kenji Watanabe, Takashi Taniguchi, Pablo Jarillo-Herrero. Electric Field Tunable Correlated States and Magnetic Phase Transitions in Twisted Bilayer-Bilayer Graphene, arXiv:1903.08596

Contents

Chapter 1

Introduction

In this first chapter, we will contextualize the work I contributed to in Pablo Jarillo-Herrero's lab. Section 1.1 presents an overview of the field of two-dimensional materials and how it evolved since the discovery of graphene. Then, we will introduce a new platform called magic angle twisted bilayer graphene in Section 1.2, which was originally designed to induce and study strongly correlated physics.

The discussion about magic angle graphene will naturally raise the question whether strongly correlated physics can also be observed in similar systems. At this point, 'twistronics' will be presented as a new field that studies Moiré systems exhibiting strong correlations. This project focuses on one of the Moiré platforms that have been recently reported, twisted bilayer-bilayer graphene. In Section 1.3, we will introduce this new van der Waals heterostructure and study its behavior based on theoretical considerations and numerical calculations.

1.1 2D materials and van der Waals heterostructures

In 2010, Andre Geim and Konstantin Novoselov were awarded the Nobel Prize in Physics for their groundbreaking discovery back in 2004: they were able to isolate graphene, a single layer of graphite. For the first time in history, researchers had

found a material that was only one atom thick, proving that a whole new regime of physics could be accessible. Further, the unique properties of graphene could have a wide variety of applications in industry.

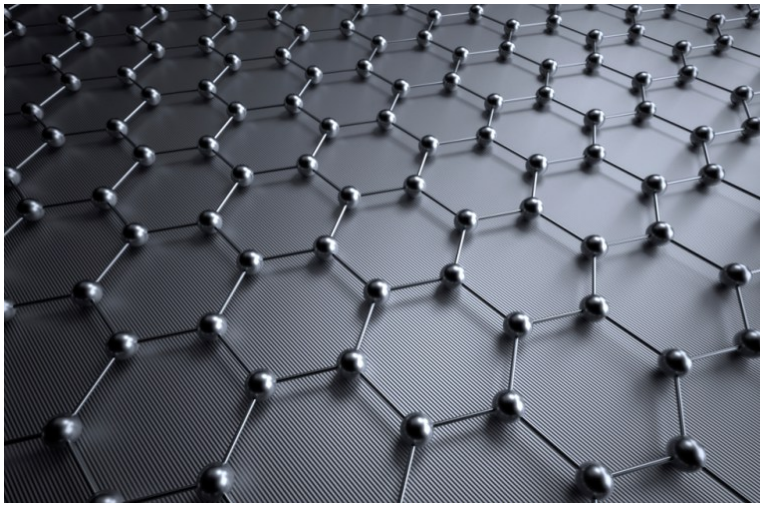

Figure 1-1: Representation of a graphene sheet.

Graphene was thoroughly studied and characterized during the next years. As an atomically thin allotrope of carbon, it just consists of carbon atoms forming a two-dimsensional (2D) honeycomb lattice, as depicted in Fig. 1-1. Graphene is transparent and flexible, but at the same time incredibly strong. In addition, it possesses the highest thermal conductivity measured and can conduct electricity better than copper. In terms of its electronic band structure, graphene shows a linear dispersion near the K and K' points. As a result, this material has no energy gap and its charge carriers can be described as massless, meaning that their nature can be better described using Dirac equation than Schrödinger's one. This is why these quasiparticles are referred to as massless Dirac fermions and the band structure features at the K and K' points are known as Dirac cones.

However, graphene is not the only two-dimensional material that can be isolated. There is a huge variety of bulk crystals that have a 2D counterpart. These new 2D materials can possess many different properties: from being an electrical conductor as graphene, to an insulator as hexagonal boron nitride (hBN) or a semiconductor such as the transition metal dichalcogenides.

Apart from studying the individual properties of each material, this whole range of 2D crystals also offers a new possibility: one can think of stacking different 2D materials on top of each other to produce new structures with very different behaviors. These stacks are called van der Waals heterostructures and offer a playground that is only limited by our imagination [1] [2].

1.2 Magic angle graphene: A pathway to Twistronics

As we have seen, 2D materials can be stacked on top of each other to create new structures. This is the reason why this field has been often referred to as Lego land. However, this analogy is not completely accurate. While Lego pieces can only be stacked on top of each other with a very specific alignment, 2D materials can be rotated with respect to each other. In other words, one has an extra degree of freedom to play with: the twist angle between layers (a more precise explanation of the method used to obtain a certain twist angle will be given in Section 2.2). This is a very unique feature of 2D materials, which can be mechanically exfoliated and then placed on top of each other in any configuration, something that does not occur with bulk materials or even 2D crystals grown by molecular beam epitaxy.

If chosen wisely, the twist angle between layers can give rise to very interesting and new physics. The paradigmatic example is now 'magic angle graphene' (MAG), a platform that has revolutionized physics since it discovery in 2018 [3] [4]. MAG is based on two graphene layers that are rotated with respect to each other by a specific angle of around 1.1°, the so called 'magic angle'. This system is also referred to as 'twisted bilayer graphene'.

The first prediction of the magic angle was done by Rafi Bistritzer and Allan MacDonald in 2011 [5] (see also Ref. [6]). They realized that two periodic patterns overlaid with a certain twist angle (forming a structure known as Moiré pattern) lead to a strong coupling between both layers, much stronger than if they were not twisted.

To describe MAG or twisted double-layer graphene, as MacDonald called it at that time, a continuum model Hamiltonian that contained three different terms was used: two single-layer Dirac Hamiltonian terms that represent each of the two graphene layers and a tunneling term that describes the coupling via tunneling between both sheets. The study concluded that, for a discrete set of magic angles, the renormalized Fermi velocity at the Dirac points vanishes (the magic angle of 1.1° mentioned before is the largest of this set of magic angles). As a result, the lowest bands of the Moiré system flatten and the density of states at the Dirac points gets enhanced for these specific angles. This flattening of the bands is crucial, as it is supposed to give rise to strongly correlated interactions between the electrons in the material. Since this first prediction and specially after the experimental realization of MAG, many theoretical studies have been carried out to understand this platform better and to do more accurate predictions. For example, Ref. [7] introduces the effect of lattice relaxation in MAG, which makes AB stacking regions of the Moiré pattern expand with respect to AA regions. This results into different intra- and inter-sublattice hopping parameters. With this correction, bands flatten even more. Besides, this paper extends the study to multilayer twisted graphene superlattices, obtaining the magic angles for different configurations.

Fig. 1-2 a) shows the Moiré pattern obtained in MAG. An intuitive way of understanding how the flat band condiction is achived is shown in panels e-f). The low-energy band structure of graphene can be depicted by the Dirac cones. If the two graphene layers are rotated in real space, the Dirac wavevectors and cones in reciprocal space will be also rotated by the same angle (see Fig. 1-2 b)). The difference between these K wavevectors gives rise to the mini Brillouin zone depicted in panel b), that represents the reciprocal lattice of the Moiré superlattice. The Dirac cones shown in panel e) hybridize due to interlayer coupling, so that a band gap opens (see panel f)). If we lower the angle, the hybridization energy will increase with respect to the kinetic energy and the lower hybridized states will be pushed down to lower energies. As a result, the flat bands depicted in panel g) will be formed. Fig. 1-2 d) shows a numerical calculation of the band structure using a tight-binding model.

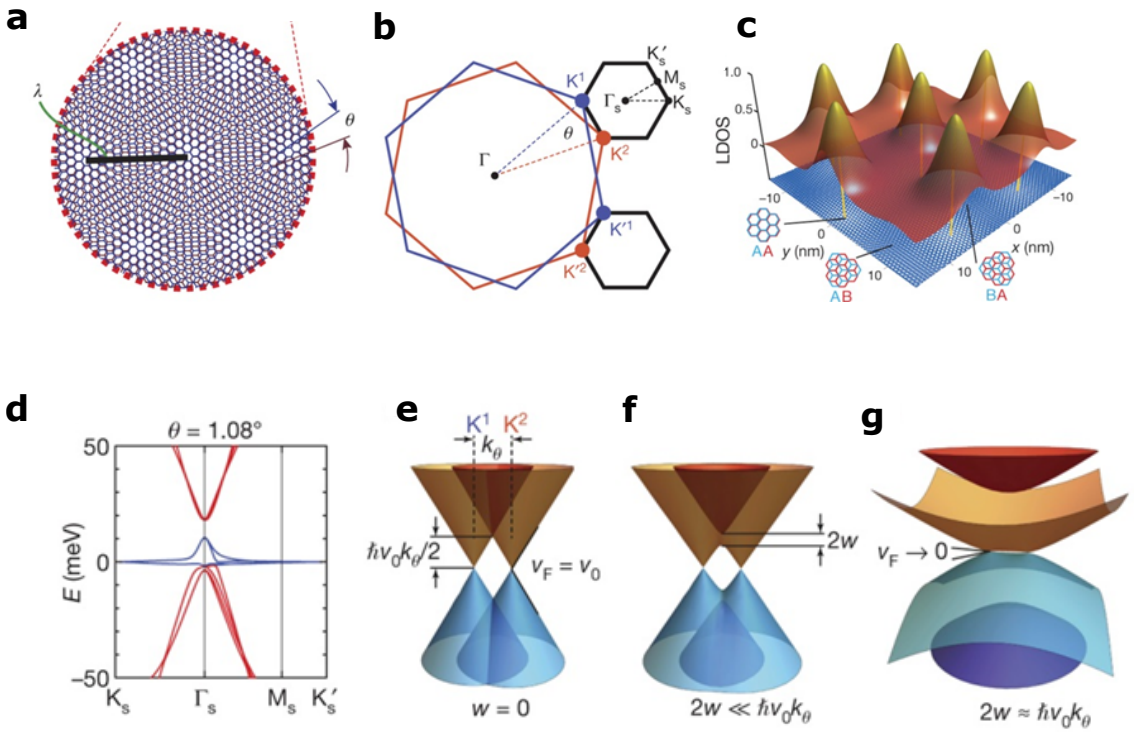

Figure 1-2: (a) Moiré pattern seen in MAG. (b) Brillouin zones for the two twisted graphene layers (red and blue). Mini Brillouin zone constructed from the difference between the two K wavevectors of the different layers (black). (c) Local density of states for $\theta = 1.08°$. Electron denity is concentrated in the AA-stacked regions. (d) Band energy for MAG with $\theta = 1.08°$ computed with a tight-binding model. (e)-(g) Effect of interlayer coupling and angle reduction on the two displaced Dirac cones, leading to band flattening. From Ref. [3].

Nearly flat bands with a bandwidth of around $12meV$ are obtained for a twist angle between layers of $\theta = 1.08°$. Finally, Fig. 1-2 c) shows the profile of the density of states in MAG. As we can see, the electrons are highly concentrated in the AA stacking regions, with almost no wavefunction amplitude in the AB or BA regions (panel c) also includes illustrations of the configurations of carbon atoms in each stacking region). Note also that for small twist angles, the electronic bands of the mini Brillouin zone have a four-fold degeneracy (valley and spin). As a result, we reach the first band insulator when there are 4 electrons per Moiré unit cell in the system. We will refer to the corresponding carrier density as superlattice density $n_s = 4/A$, where A is the area of a Moiré unit cell [3].

The structure of the MAG devices measured in Ref. [3]-[4] is similar to the one

described in Chapter 2, Fig. 2-1. The twisted bilayer graphene, that originates from the same flake (see Section 2.2), is encapsulated with hexagonal boron nitride (hBN) flakes. The encapsulated stack is etched with the form of a hall bar and gold metallic contacts are evaporated, so that one can voltage- or current-bias the sample and measure the longitudinal and transverse voltage drop at the same time. Additionally, there is a bottom gate that allows to change the carrier density in the device. In other words, it modifies the number of electrons (or holes) responsible for electronic transport (a more accurate description of the fabrication process is done in Chapter 2).

The two-probe conductance (measurement technique that consists on using the same two contacts to bias the sample and measure its voltage drop) for one of the two devices studied in Ref. [4] is shown in Fig. 1-3 a). First, the usual V-shape conductance for graphene is observed near charge neutrality (zero carrier density). We can see how the conductance goes to zero at the superlattice density $n = \pm n_s$, indicating the presence of the superlattice gap. As discussed above, these insulating states correspond to filling the superlattice unit cell with ± 4 electrons and are therefore expected in the single particle picture. More interestingly, we also observe conductance minima for ± 2 and ± 3 electrons per unit cell. These minima correspond to many-body gaps that are induced by the competition between Coulomb and kinetic energy as a result of the localization of electrons at the magic angle configuration. In other words, they are correlated insulators (it is generally considered that these insulating states are Mott insulators, although it is not yet completely clear whether this is the case).

The correlated insulator at half the superlattice density can be also seen in Fig. 1-3 b-c) for two different samples with different angles, $\theta_1 = 1.16°$ and $\theta_2 = 1.05°$. The insulators correspond to the dark red region in the central part of the maps and are labeled as 'Mott'. Upon electrostatic doping (with the bottom gate) away from the correlated insulator at $n = n_s/2$, two superconducting domes appear (dark blue regions). The superconducting transitions are plotted in Fig. 1-3 d) at optimal doping for both samples. An extra proof for superconductivity is shown in panel e).

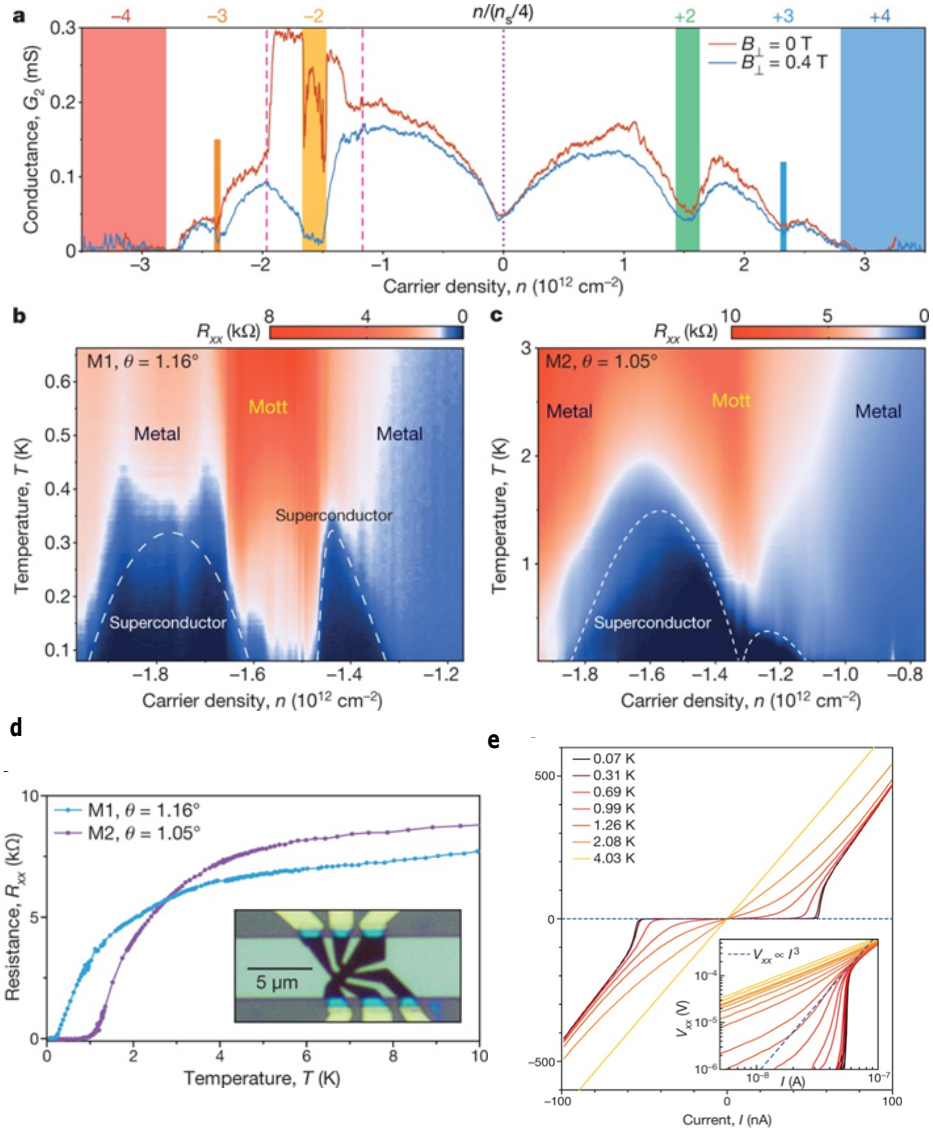

Figure 1-3: (a) Two-probe conductance for device M1 ($\theta = 1.16°$) at zero and finite perpendicular magnetic field. The superlattice band gaps are shown at $n = \pm n_s$. Correlated insulators are shown at $n = \pm n_s/2$ and $n = \pm 3n_s/4$. A conductance peak on both sides of $n = -n_s/2$ appears for zero magnetic field and vanishes when increasing the field. (b) Four probe resistance R_{xx} for device M1 as a function of carrier density and temperature. Correlated insulator centered at $-n_s/2 = -1.58 * 10^{12} cm^{-2}$, with superconducting domes at each side. (c) Same as (b) for device M2 ($\theta = 1.05°$). (d) Superconducting transition for devices M1 and M2. (e) I-V curves for device M2 at optimal doping $n = -1.58 * 10^{12} cm^{-2}$ at $70mK$. From Ref. [4].

The I-V curves inside the domes have a non-linear behavior, showing a critical current below which no voltage drops across the sample, while the behavior turns ohmic in the metallic phase outside these domes.

A similar behavior is observed if one applies a perpendicular magnetic field. Fig. 1-4 shows traces at several carrier densities near half-filling ($n = n_s/2$). For zero magnetic field (panel a)), we observe a resistance increase at around $4K$ for those densities that exhibit the correlated insulating state. At around $1K$, a superconducting transition to zero resistance takes place for all depicted densities. When applying a small perpendicular magnetic field of $B = 0.4T$, the superconducting transition disappears (panel b)). One obtains a critical magnetic field of around 70mT. If we keep on increasing the magnetic field, a superconductor/insulator to metal transition is induced, as depicted in panel c).

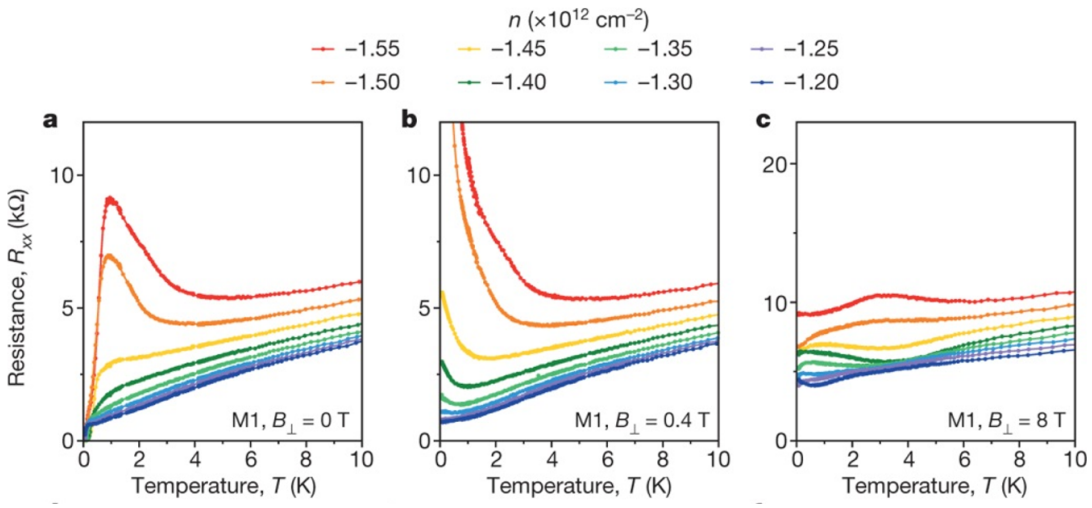

Figure 1-4: $R_{xx} - T$ traces for sample M1. The density range plotted includes the correlated insulator at $-n_s/2$ and the superconducting dome located at slightly larger densities. (a)-(c) show the behavior at different perpendicular magnetic fields. From Ref. [4].

A more thorough study of the dependence of the insulating state at half-filling with in-plane magnetic field, done in Ref. [3], shows how the insulator is probably spin-singlet. In other words, after the gap at half-filling is opened, the application of en external magnetic field polarizes the excitations in each formed band according to their spin. The gap therefore closes as a result of the Zeeman effect until conduction is allowed again and the system transitions to a metal.

It is worth pointing out that the Shubnikov-de Haas oscillations were also mea-

sured for sample M2 in order to obtain the effective mass and effective density by means of the Lifshitz-Kosevich formula. The corresponding data, published in Ref. [4], will be used in this work in Appendix A to study the the strange metallic behavior exhibited by MAG.

The original phase diagram for MAG is depicted in Fig. 1-5. The y-axis shows the temperature of the system and the x-axis the filling, which is related to the carrier density. The filling ν is the amount of charge carriers per Moiré unit cell. In other words, $\nu = 4$ is the same as the superlattice density n_s. The phase diagram shows the following phases:

- Charge neutrality point at $\nu = 0$ (dark blue).
- Band insulators at $\nu = \pm 4$ (green).
- Correlated insulators at $\nu = \pm 2$ or half the superlattice density (light blue).
- Four superconducting domes, one on each side of each of the correlated insulators (orange).

Since the first realization of MAG, this phase diagram has been continuously evolving. In Ref. [8], ferromagnetism near three-quarters the superlattice density is reported. Also, nematicity in the superconducting state has already been identified by Yuan Cao [9]. In Jarillo-Herrero's group, I have been also studying the strange metallic behavior of MAG at certain fillings. This work has resulted into a publication, Ref. [26]. In Appendix A, we explain the nature of this strange metallic phase. Researchers at ICFO have also reported a MAG sample that exhibits more correlated insulators and superconducting domes than the ones shown in Fig. 1-5. Also, a lot of effort has been done to study the effect of other parameters. For instance, Ref. [11] shows that the magic angle condition can be tuned by applying pressure as a result of the modified interlayer coupling between graphene sheets.

MAG has attracted the interest of many physicists since it was first experimentally realized. First, it offers a unique playground to study strongly correlated physics. Thanks to its unprecedented versatility and tunability (one can explore the whole

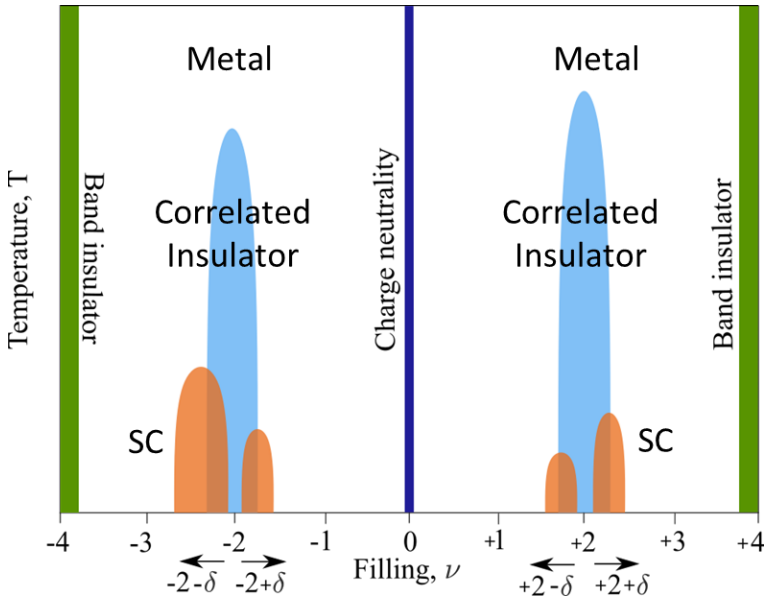

Figure 1-5: Initial phase diagram of MAG. The x-axis represents the filling ν of the superlattice unit cell. $\nu = -4$ and $\nu = 4$ stand for 4 holes or electrons, respectively, per Moiré unit cell. The y-axis represents the temperature of the system. Charge neutrality ($\nu = 0$), the band insulators ($\nu = \pm 4$), the correlated insulators at half the superlattice density ($\nu = \pm 2$) and the superconducting domes nearby are depicted.

carrier density range by just modifying the voltage applied to the bottom gate of the device), it could shed light to high-T_c superconductors such as cuprates, where the carrier density cannot be modified once one has grown the crystal.

But, perhaps more importantly, MAG has created a completely new field: twistronics. Twisting between layers and flat band engineering is not exclusive of MAG. Instead, one can think of doing the same with many other materials to induce correlations that where not present in the 'untwisted' building blocks. The wide variety of 2D materials and the many different behaviors they present (insulators, metals, semimetals, semiconductors, superconductors, magnets, quantum spin liquids) can unveil novel electronic states and make this field immensely fruitful. In fact, there is already ongoing research in this direction and other Moiré systems showing correlated physics, such as ABC trilayer graphene on hBN [12], twisted bilayer WSe_2 [13] or twisted bilayer-bilayer graphene [14] [15] [16], have been already realized. In this work, we will focus on the latter system.

1.3 Twisted bilayer-bilayer graphene

In this work, we study a new Moiré superlattice, small-angle twisted bilayer-bilayer graphene (TBBG). It consists on two sheets of bilayer graphene rotated with respect to each other by an angle near to 1.1°, as shown in Fig. 1-7 a). Thus, we have a total of four graphene layers in our system.

1.3.1 Bilayer graphene

As the basic building block for TBBG, bilayer graphene (BG) will have a great effect on the properties of this Moiré superlattice. Bilayer graphene is usually found in the AB or Bernal-stacked form. For this configuration, half of the Carbon atoms of the upper graphene layer are located in the center of the hexagons defined by the lower one, as shown in Fig. 1-6 a).

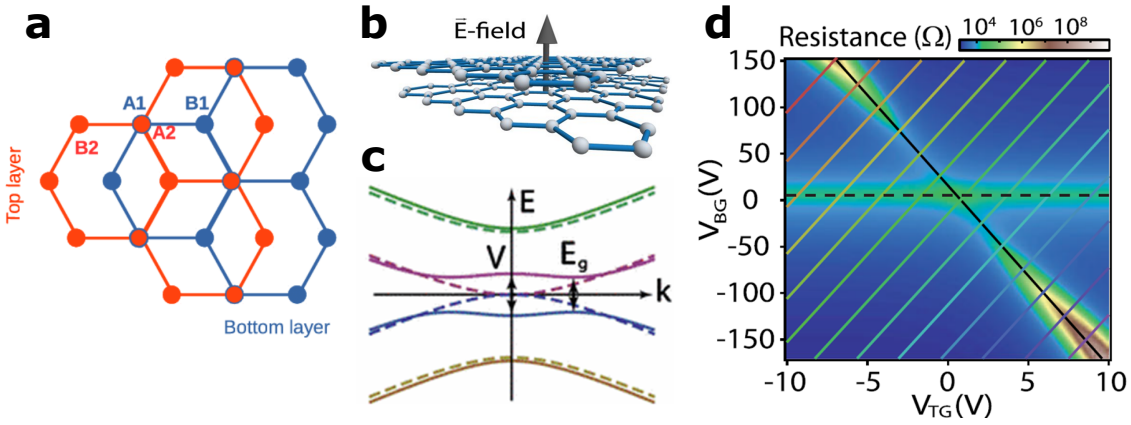

Figure 1-6: (a) Schematic representation of Bernal-stacked or AB bilayer graphene. Half of the Carbon atoms of the upper graphene layer (orange) are located in the middle of the hexagons defined by the lower one (blue). (b) Electric field applied across the stack, which creates a potential difference between the two layers. (c) Band structure of AB bilayer graphene without electric field (dashed lines) and with displacement field (solid lines). (d) Resistance of AB bilayer graphene as a function top and bottom gate potential. The solid black line represents the displacement field axis. From Ref. [17].

The band structure of bilayer graphene is very different from that of graphene. Instead of having a Dirac cone at the K points, the energy dispersion takes the form shown by the dashed lines in Fig. 1-6 c). It is still gapless at zero energy, but the

dispersion relation is parabolic. When an electric displacement field perpendicular to the plane defined by the 2D material is applied (see panel b)), a band gap opens at zero energy (or charge neutrality), resulting in the band structure depicted by the solid lines.

Fig. 1-6 d) shows this gap opening. The resistance drop across a bilayer graphene sample is plotted as a function of top and bottom gate potential. Tuning the top and bottom gate voltages enables us to modify the carrier density and displacement field across the sample (see Chapter 2). The solid black line, located at zero carrier density or charge neutrality, represents the displacement field axis. For zero displacement field and zero carrier density ($V_{tg} = V_{bg} = 0$), the sample shows a conductive behavior. However, if the displacement field is increased, the resistance increases due to the formation of a band gap [17].

1.3.2 Twisted bilayer-bilayer graphene

If one takes two sheets of untwisted Bernal-stacked bilayer graphene and stacks them together with a relative angle θ, one can build a completely new system called twisted bilayer-bilayer graphene (TBBG), shown in Fig. 1-7 a). This Moiré structure has not been studied as deeply as MAG, although some theoretical results have already appeared since its first experimental realization in March 2019. We will not do a thorough theoretical analysis of the system here, but the reader may refer to Ref. [18] for a deeper theoretical framework.

Instead, we will try to understand the basic features of TBBG using a much simpler and intuitive argument, similarly to what was done for MAG in Fig. 1-2 e-g). Fig. 1-7 e-g) shows the analogous reasoning for TBBG. As seen in the previous subsection, bilayer graphene has a parabolic energy dispersion at the K points. Due to the rotation in real space between the bilayer sheets, the corresponding parabolic bands are displaced in momentum space as shown in panel e). We can see how the bands cross, meaning that we are not considering any coupling between bilayer sheets in the problem. Similarly to what happened in MAG, the bands hybridize if we introduce interlayer coupling or, in other words, if the two bilayer graphene

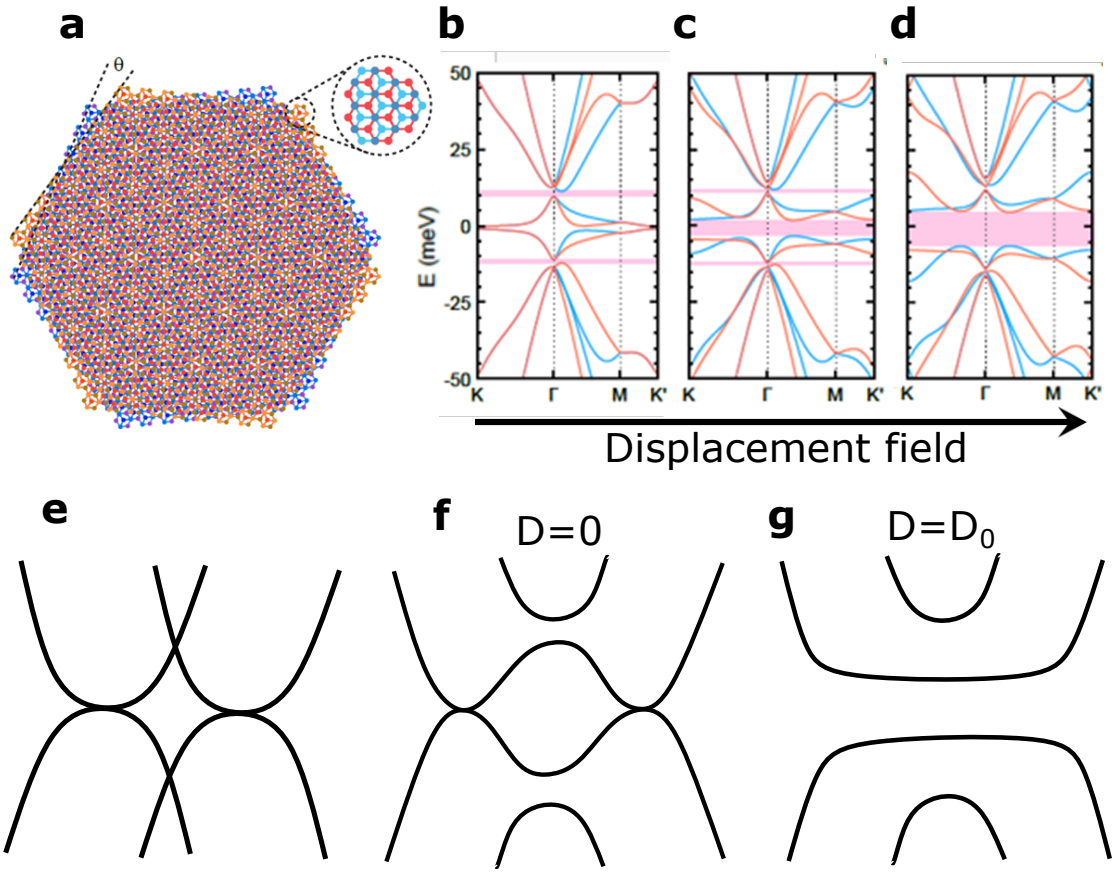

Figure 1-7: (a) Representation of TBBG, which consists of two sheets of AB bilayer graphene rotated by a twist angle θ. (b)-(d) Calculated band structure for TBBG with $\theta = 1.23°$ using a continuum model. The applied displacement field is considered to create the same voltage difference between all graphene layers. The potential difference between layers is $\Delta V = 0$ for (b), $\Delta V = 6mV$ for (c) and $\Delta V = 12mV$ for (d). (e) Schematic representation of the band structure of TBBG at the K points when no interlayer coupling is considered. (f) Hybridization of the bands in (e) due to interlayer coupling. (g) Flatening of bands when an electric displacement field is applied.

sheets start interacting with each other. As a result, gaps will open at the crossings, as depicted in panel f). At this point, we would start reducing the angle for MAG so that the bands flatten and the magic angle condition is reached. However, we have an extra knob to tune in TBBG, which was inhereted from its building block, bilayer graphene. One can modify the band structure by applying an external electric displacement field D. If one does so, gaps will be opened at zero energy and the lower bands will naturally become flatter, at least for a certain range of displacement

fields. This effect is shown in panel g). As we will see, this characteristic of bilayer graphene will introduce some differences between the behaviors exhibited by TBBG and MAG. Apart from acquiring a displacement field tunability, this extra knob provides a huge advantage: one does not need to rely anymore on hitting a very specific angle, as one can engineer flatter bands by just applying an external field. This should result in a wider range of angles showing correlated physics, as shown in Ref. [14], where correlated phenomena are observed in samples with twist angles ranging from $\theta = 1.23°$ to $\theta = 0.84°$.

In Fig. 1-2 b-d) we show real simulations of the band structure of TBBG for a sample with twist angle $\theta = 1.23°$ using a simple continuum model [14]. More precise calculations need to be performed, but these band structures already catch the essence of the behavior of TBBG. If no displacement field is applied (panel b)), the bands have a relatively large bandwidth and a gap is present at the superlattice density of the system, which corresponds to four electrons per Moiré unit cell. Panel c) shows what happens when a finite displacement field is applied. A gap opens at zero energy, as expected for bilayer graphene. Also, the gaps at $\pm n_s$ seem to reduce and the bands become slightly flatter, giving rise to strongly correlated physics. If we keep on increasing the electric field across the stack, the gap at zero energy gets enhanced, while the superlattice gaps disappear. Additionally, the bandwidth increases again.

The rest of the work is organized in the following way: in Chapter 2, we will discuss the structure of the TBBG devices and the different fabrication steps needed to produce them; in Chapter 3, we will review the working principle of the dilution refrigerator (the experimental equipment used to measure the samples) and we will study and characterize the behavior of this Moiré superlattice; finally, a brief conclusion will be done in Chapter 4.

Chapter 2

Sample fabrication

In this chapter, we will explain how TBBG samples are fabricated. In general, the fabrication technique is similar to the one described in Ref. [3] and [4] for MAG. The fabrication process can be divided into three parts: first, a gold backgate is evaporated and a bottom hexagonal boron nitride (hBN) flake is transfered on top; second, the stack consisting of two bilayer graphene flakes rotated with each other is done and deposited on top of the gates; finally, gold contacts are evaporated and the geometry of the final device is defined by etching processes. This chapter is therefore organized in three sections, each of them focusing on each of the parts mentioned.

Before describing the different steps, we can first take a look at how a finished device looks like. Fig. 2-1a) shows a schematic representation of the final device, whereas Fig. 2-1b) is an optical image of one of the samples produced. The whole device is fabricated on top of a $Si0_2/Si$ substrate. The TBBG is encapsulated between two hBN flakes, which are depicted as blue and green surfaces in the schematic representation. In the optical picture, the whole stack has a green/blue color. We also have three gold contacts at each end of the device. The four lateral contacts are generally used to measure the longitudinal R_{xx} and transverse resistance R_{xy} across the device, while the two others are employed to apply a voltage or a current through the sample. It must be added that the function of each of the contacts can vary (e.g. one can use one of the lateral ones to voltage-bias the sample), although in those cases the Hall-bar geometry of the sample is lost.

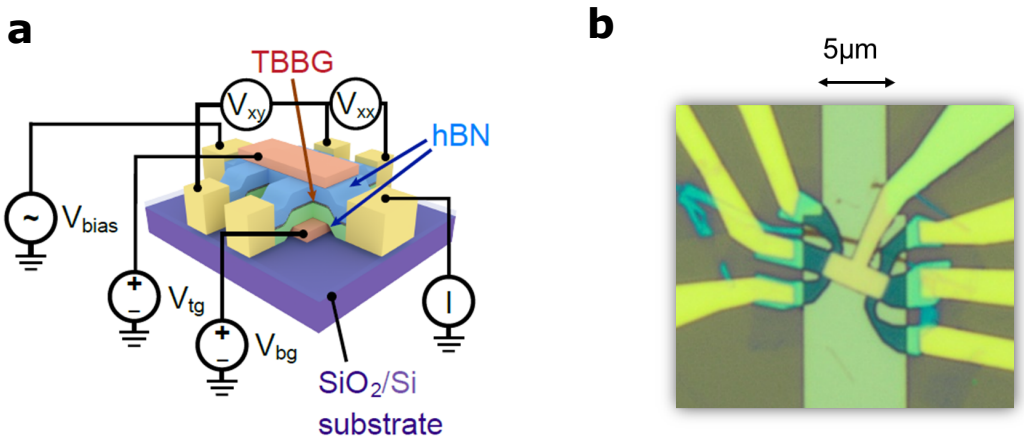

Figure 2-1: Final geometry of the TBBG devices. (a) Schematic representation of the device. The top and bottom gates are depicted in red. The yellow cubes stand for the six evaporated contacts in the device. Two of these contacts correspond to the drain and the source used to bias the sample, while the others are used to measure R_{xx} and R_{xy}. The blue and green layers are the top and bottom hBN flakes respectively, while the TBBG lies in between. (b) Optical image of a real sample, containing the same elements enumerated in (a).

Finally, each sample has a top gate and a bottom gate. The bottom gate is the big, vertical metallic contact that can be seen in the optical picture; the top gate is the gold piece that covers the whole device. When applying a voltage to them, one can modify the number of carriers in TBBG and create an electric displacement field across the sample. One can think of it as a parallel plate capacitor: if the same potential is applied in both plates, no field is induced but the material lying in between is doped; on the other hand, when we apply voltages of the same value but opposite sign, an electric field is created and no charge carriers are induced in the material (this is true in the absence of impurities and if the top gate capacitance c_{tg} and the bottom gate capacitance c_{bg} are identical, meaning that the bottom and top hBN flakes are equally thick). The charge carrier density n and the displacement field D are related to the top and bottom gate voltages by the following equations

$$n = [c_{tg}(V_{tg} - V_{tg,0}) + c_{bg}(V_{bg} - V_{bg,0})]/e$$
$$D = [-c_{tg}(V_{tg} - V_{tg,0}) + c_{bg}(V_{bg} - V_{bg,0})]$$

where e is the elementary charge and we are accounting for offsets in the voltages due to impurtity doping. Note also that this formula just represents a rotation.

2.1 Bottom gate and bottom hBN

2.1.1 Evaporation of the bottom gate and markers

The first step to fabricate TBBG samples with metallic top and bottom gates consists on evaporating the bottom gate and the markers on a $Si0_2/Si$ substrate. Note that the bottom gate does not necessarily need to be metallic, but could also be a graphite crystal in which case this step would be modified.

Before evaporating the metal, one needs to define the desired pattern on the sample. In order to do so, the electron-beam (e-beam) lithography technique is used. It consists on scanning a focused beam of electrons on our sample to draw nanometric shapes. The surface of the sample must be covered with an electron-sensitive resist. When the electron beam impinges on it, the resist undergoes a chemical reaction and its solubility changes. Then, one just needs to immerse the chip in a solvent, so that the exposed part of the resist gets dissolved. As a result, the chip underneath gets uncovered. In our case, we use a double resist layer consisting of PMMA (PMMA950A2 on top and PMMA495A5 at the bottom). The resist is deposited on the sample using a spin coating technique.

Afterwards, the metallic bottom gate and markers are evaporated on top of the patterned resist. A thermal evaporation process is used: inside a vacuum chamber, the desired metal is heated by applying current through it until the surface atoms have enough energy to leave it. This directional beam of emitted particles is then directed onto the sample, that gets covered by it. For our TBBG samples, we first evaporate a thin layer of chromium that serves as a sticky substrate for the real metallic gate, consisting of around $30nm$ of palladium and gold (Pd/Au).

At this point, we have Pd/Au both on top of the patterned regions and on top of the resist that had not been dissolved. We then do a lift-off to eliminate the latter one. This process consists on putting the sample in acetone for more than three hours and rinsing the sample with either IPA or acetone afterwards until the resist and the metal on top of it detach from the surface of the chip.

The final result can be seen in Fig. 2-2 . The bottom gate is the vertical contact

in the center of the image. The pattern circling it, as well as the shapes located at the four edges of the picture, are the markers of the device. They are used for alignment purposes (e.g. during e-beam lithography).

Figure 2-2: Evaporated markers and bottom gate.

2.1.2 Obtaining of hBN (and graphene)

All 2D flakes where obtained using micromechanical exfoliation, also known as 'scotch tape technique' (this is the method used by Geim and Novoselov to obtain the first graphene flakes). The working princple is very simple: one places a small piece of crystal onto a sticky tape and folds and peels the tape several times to create thinner and thinner layers of the crystal.

Once the flakes are thin enough and the tape is sufficiently dense, it is placed on top of a previously cleaned $Si0_2/Si$ chip. In general, we heat the chip on a hotplate at $180°C$ during 30 seconds so that the crystals stick better to it. After several minutes, the tape is removed and the flakes are transfered onto the chip. Note that this last step acts as an extra peeling process, meaning that only a part of the flakes will be deposited on the substrate.

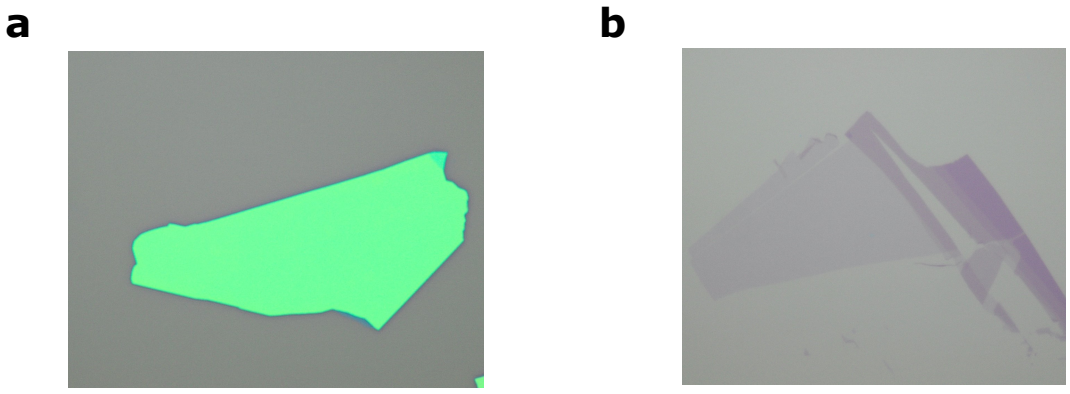

Figure 2-3: (a) Mechanically exfoliated hBN flake. (b) Mechanically exfoliated graphene flake.

Fig. 2-3 shows two micromechanically exfoliated flakes, an hBN one in panel a) and a graphene one in b).

Finally, I would like to mention that chips with exfoliated hBN are also annealed to clean and flatten the flakes and to get rid of glue residues. The heat cleaning is done in a furnace with a continuous flow of a mixture of argon and hydrogen. The process takes place at $500°C$ during around 9 hours. Heat cleaning is not done with exfoliated graphene flakes because graphene wraps up when being heated.

2.1.3 Transfer

Finally, we need to deposit an hBN flake on top of the bottom gate of the device. This process is performed using a transfer setup. It consists of a stage which is used to hold a chip and is mounted on top of a floating table to avoid vibrations. The stage can be moved using micro-manipulators. A microscope is mounted on top of that to have optical control of the process. Additionally, there is a slide holder to the right of the stage. Thanks to it, one can bring glass slides in between the chip on the stage and the objective. This holder also has micro-manipulators, so that its position in the horizontal plane can also be controlled. Besides, it has a motor acting on the z-direction, which allows to bring the surface of the glass slide in contact with the chip.

To transfer flakes, we use polycarbonate (PC) slides. It consists of a glass slide,

on which a small piece of polydimethylsiloxane (PDMS) is deposited. We use this material as a soft cushion that allows a smooth contact with the flakes on the chip. On top of the PDMS, a thin layer of PC is placed. This polymer is sticky and is used to pick up the flakes from the chip.

Figure 2-4: hBN flake on top of the botton gate.

We can now describe how the transfer is done:

1. hBN pick-up: we first place a chip with exfoliated hBN on the stage and heat it up until it reaches a temperature of around $100°C$. Then, we lower the PC slide until it touches the chip and the flake is picked up. We then raise the PC slide, which now has the flake.

2. Transfer on top of the bottom gate: we place the chip with the evaporated gates on the stage and bring the PC slide with the picked-up hBN in contact with the gate. By heating up the chip to $160°C$, the PC melts and both the flake and the PC get deposited on the chip.

3. Afterwards, we put the chip in chloroform for several minutes until the PC gets completely dissolved.

An example of the final result is shown in Fig. 2-4.

2.2 Stacking

Now that we have the bottom gate with the bottom hBN, we have to finish the van der Waals heterostructure. We thus need to stack the two sheets of bilayer graphene together (rotated by the desired twist angle), encapsulate them with the top hBN flake and transfer the whole stack on top of the bottom hBN.

The crucial step in this process is to create the rotated bilayer-bilayer graphene sheet. The procedure we use is analogous to the one described in Ref. [19]-[21] and is the same technique that was employed to produce the MAG devices reported in Section 1.2. We will refer to it as 'tear and stack' technique. A schematic representation of the process is shown in Fig. 2-5.

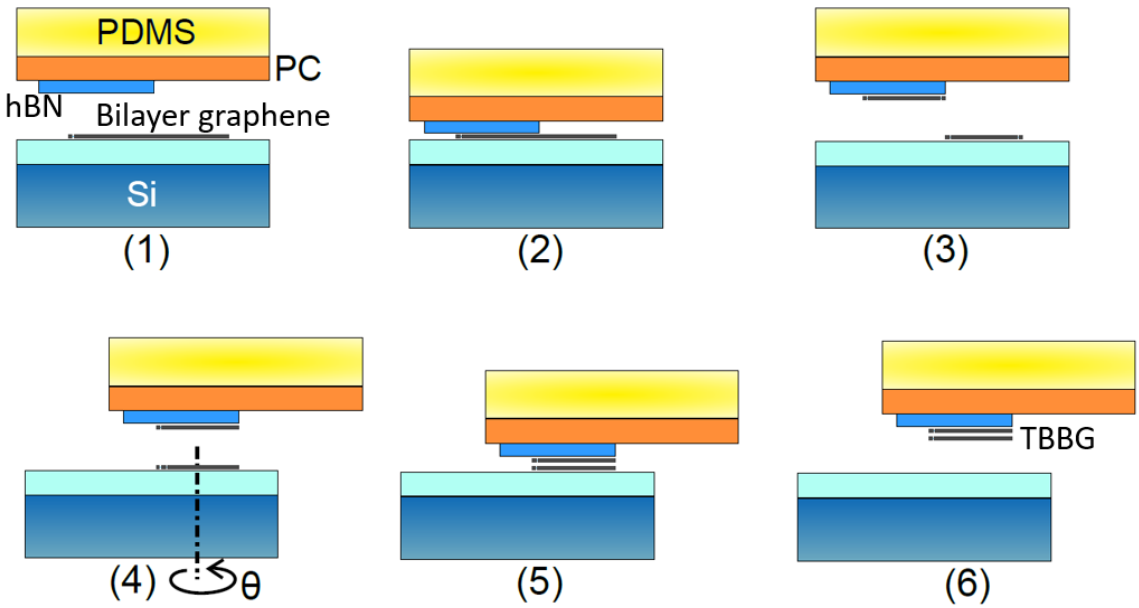

Figure 2-5: Schematic representation of the 'tear and stack' technique. A more accurate description of each step is done in the main text.

The stacking is performed as follows:

1. We first start picking up the top hBN. To do so, we use a PC slide again and follow the same procedure as described in the previous section (we also heat up the chip until it reaches a temperature of around $100°C$ for this step).

2. We then place the bilayer graphene flake on the stage (Fig. 2-5 (1)). We lower the PC slide with the top hBN flake until it touches the chip. However, the hBN does not contact the whole bilayer graphene flake but just half of it (Fig. 2-5 (2)). When we raise the PC slide, the bilayer graphene tears apart so that only half of the flake gets picked up (Fig. 2-5 (3)).

3. We then rotate the stage by the desired angle, in our case around 1.1° (Fig. 2-5 (4)), lower the PC slide again (Fig. 2-5 (5)) and pick up the second half of the bilayer graphene flake (Fig. 2-5 (6)). We now have the TBBG on the PC slide. Both pick-ups of bilayer graphene are done at room temperature.

The whole stack is then transferred on the bottom gate, which already had the bottom hBN on top. This release is done at $160°C$ so that the PC melts. Finally, we put the chip with the finished stack on chloroform to dissolve the PC. An example of a finished stack is shown in Fig. 2-6.

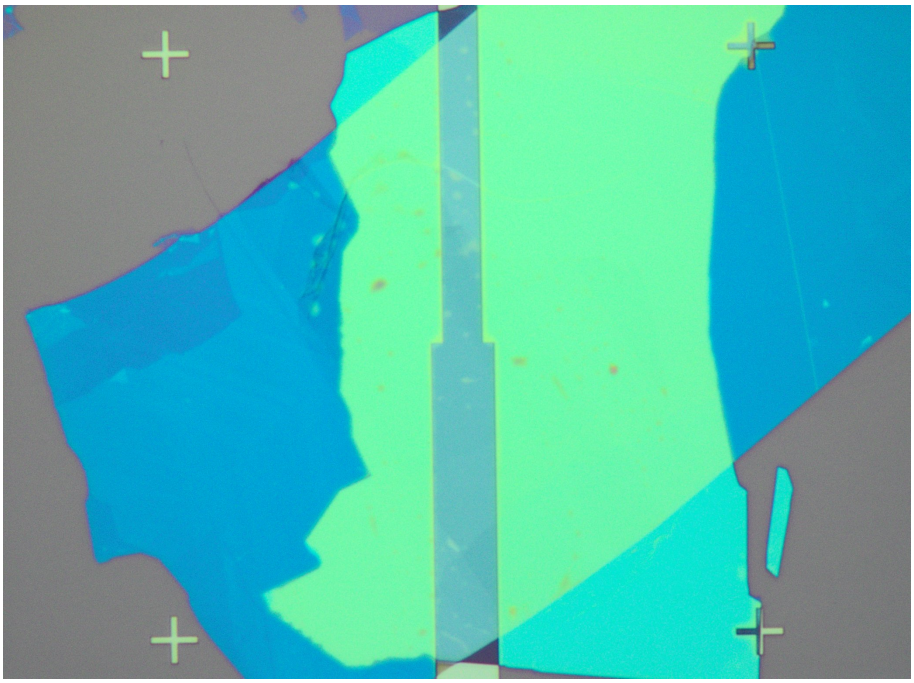

Figure 2-6: Complete stack (TBBG encapsulated by hBN) on top of a metallic bottom gate.

Note that the two bilayer sheets that form the TBBG originally come from the same flake. This is important to ensure that the crystallographic orientation of both

sheets is the same. Let us image that, instead, we had used two different flakes. As we would not know the relative orientation between them, rotating the stage 1.1° would have no real meaning. For the process to work, we need to make sure that we know their crystallographic orientations. The easiest way to do it consists on using one flake to generate the TBBG stack. In this situation, both halves will be aligned so that rotating the stage by an angle θ creates a rotation between both sheets of this same value θ. This procedure is known as the 'tear and stack' technique.

2.3 Device design

We now have the bottom gate with the whole stack on top of it. Until the end of the fabrication, we will constantly use a technique called reactive-ion etching. We will therefore briefly review its working principle before moving on with the actual fabrication.

Reactive-ion etching is a dry etching technology that uses chemically reactive plasma to remove material, in our case hBN and (multilayer) graphene. The equipment consists of a vacuum chamber, where a wafer with the samples is introduced. Afterwards, gas molecules enter the chamber and an applied oscillating electric field ionizes them, creating the plasma. Because of the presence of the oscilalting field, electrons are accelerated up and down in the chamber. Some collide with the wafer, creating a negative charge that induces a negative voltage with respect to the positively polarized plasma. As a result, positive ions tend to accelerate towards the wafer and collide with the materials on the surface of the chip. If the composition of the gas is chosen properly, these accelerated ions can eliminate the material through a chemical reaction. An important property of dry etching is the fact that the ions are accelerated vertically towards the sample, producing very clean and anisotropic etching profiles, something that does not occur with wet etching technologies. If we want to etch our sample, we have to go over the same procedure as for the evaporation of the bottom gate: first, we have to spin-coat resist on top of the sample (in this case, we use PMMA950A5); then, we define the area we want to etch using e-beam lithog-

raphy; after removing the exposed resist by using the appropriate solvent, we can use the etching tool. In general, we will use two different recipes (each one consisting of different gases), one to etch hBN and another to etch multilayer graphene.

Going back to the fabrication of our TBBG samples, the next step consists on doing an etching process that eliminates most of the hBN flakes. Fig. 2-7 a) shows the initial stack and panel b) the result of this etching. This process is used to pin the whole stack together.

Afterwards, one needs to evaporate the gold contacts used to measure the sample. The resist used to spin-coat the chip is a double layer of PMMA950A2 (top) / PMMA495A5 (bottom). We use two resist layers so that the residual gold gets lifted off easier. After defining the paths of the contacts using e-beam lithography, an etching is done to remove the hBN flakes that lie in that path. Finally, the thermal evaporation is done: we first evaporate a 2nm thick chromium layer that serves as a sticky substrate for the 70nm thick evaporated gold contacts. The result can be seen in Fig. 2-7 c-d). If we look carefully at panel d), we can see how the gold contacts penetrate into the remaining part of the stack (green region). The goal is to achieve one-dimensional contacts [22], depicted in Fig. 2-8, where the metallic gate only contacts the van der Vaals heterostructure via a one-dimensional line, also referred to as edge (this procedure, developed in 2013, outperforms previous techniques such as surface contacts). In order for the contacts to work well, the metal needs to contact a clean graphene region. This is the reason why we etch an extra piece of stack and don't evaporate the metal directly at the edge defined by the first etching, which has been exposed and is not perfectly clean any more.

Panel d) also shows how the contact that corresponds to the top gate ends far away from the bottom gate, where the final device will be. Please note that the top gate should end on top of the device, as shown in Fig. 2-1, so that one can tune the carrier density and displacement field in the sample. The evaporation of the final part of the top gate is done in a separate step and the result is shown in panel e). We could not evaporate the end of the top gate with the rest of the contacts because of the etching process we did in the previous step. While we wanted to get rid of the hBN

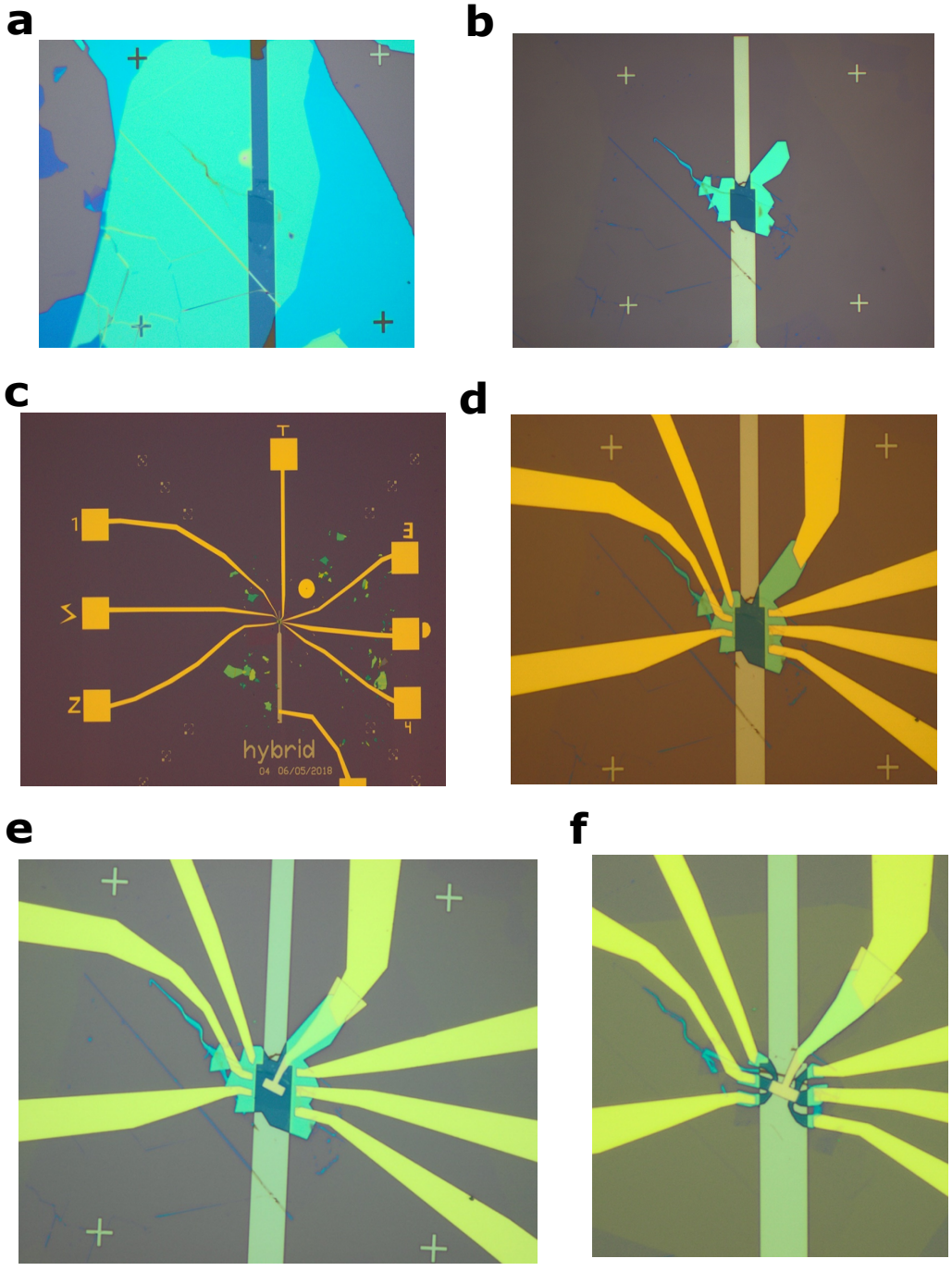

Figure 2-7: (a) Original stack on top of the bottom gate. (b) Step 1: broad etching of hBN flakes. (c)-(d) Step 2: evaporation of gold contacts. (e) Step 3: evaporation of the top metallic gate. (f) Step 4: final etching to define device geometry.

flakes that might be in the path defined by the contacts, we want to keep the hBN and graphene in this final region. The reason is obvious: if we did an etching now, we would destroy the device. Note also that this final part of the top gate always sits

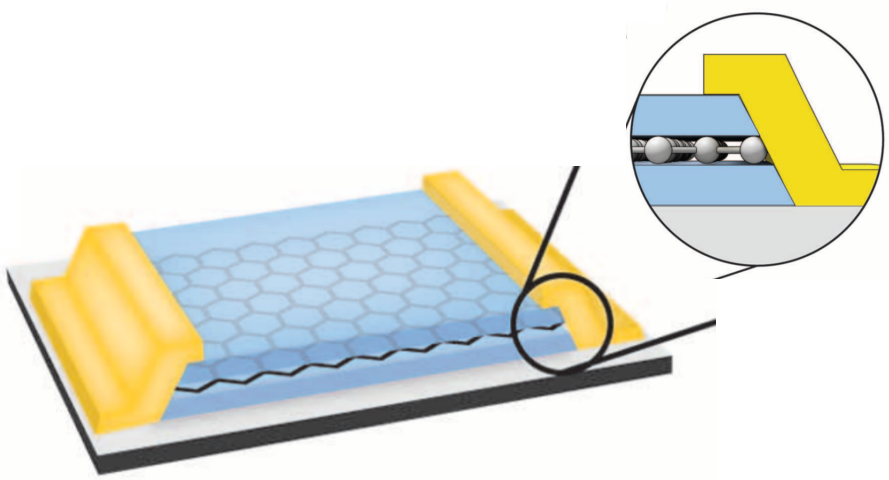

Figure 2-8: Schematic representation of one-dimensional contacts for two-dimensional van der Waals heterostructures [22].

on top of the remaining part of the top hBN flake, so that there is no short-circuit between bottom and top gate (hBN is an insulating 2D material). Additionally, one needs to ensure that the graphene flake finishes before the intersection between the final part of the evaporated top gate and the rest of the contact. Otherwise, the device and the top gate would be short-circuited. Again, the resist used is PMMA950A2 (top) / PMMA495A5 (bottom) and, in this case, the thickness of evaporated gold is considerably lower, of about 25nm.

There is only one step left, the final etching. As panel e) shows, we now have all contacts, but the geometry of the device is not well defined. In order to obtain the hall bar depicted in Fig. 2-1, we only needs to etch all the material except for the region underneath the top gate and the paths that connect the contacts with the hall bar. We use the same resist as for the broad etching, a single PMMA950A5 layer, and apply hBN and multilayer graphene etching recipes. The final result is shown in Fig. 2-7 f).

Before measuring the sample, one just needs to wire bond the device. In other words, one needs to make connections between the contact pads (big squares at the end of each evaporated contact) and the pins in the sample carrier.

Chapter 3

Measurements and results

This chapter summarizes the main results obtained when measuring our TBBG samples. First, we will briefly introduce the experimental setup used to perform the measurements in Section 3.1. Then, we will proceed to study the physics behind this twisted van der Waals heterostructure (Sections 3.2-3.4).

For this work, several samples were fabricated. However, we will only show data from one of them. This sample, which has already been reported in Ref. [14], has a twist angle of $\theta = 1.23°$.

3.1 Experimental setup

The experiments are performed in a wet dilution refrigerator. Fig. 3-1 b) shows the different parts located inside the chamber that contains the ^{4}He bath. This environment stays at an approximate temperature of $4K$. When inserting the sample inside the fridge, a little bit of ^{4}He gas is introduced inside the inner vacuum chamber, the zone where the sample resides. As a result, the sample cools to $4K$ thanks to the thermal contact with the bath.

If we only used ^{4}He, we could reach a base temperature of around $1.2K$ due to a process called evaporative cooling. In this technique, we feed a pot (often refereed to as $1K$ pot) with ^{4}He that comes from the bath. Through pumping, one evaporates the liquid and achieves the cooling through the latent heat of the evaporated fluid.

However, working with ^{4}He is not enough if we want to reach lower temperatures. To reach temperatures of around $0.3K$, one needs to add ^{3}He. Compared to ^{4}He, ^{3}He has a lower latent heat of evaporation, a higher vapour pressure and is a Fermion, whereas ^{4}He is a Boson. Let us imagine we have now a ^{3}He-^{4}He mixture. If we cool it down, it will undergo a superfluid transition. If we keep on cooling the mixture, a phase separation will occur and two different phases will emerge: a ^{3}He pure phase floating on top of a ^{4}He-rich dilute phase (at $0K$, this phase would only contain 6.4% ^{3}He).

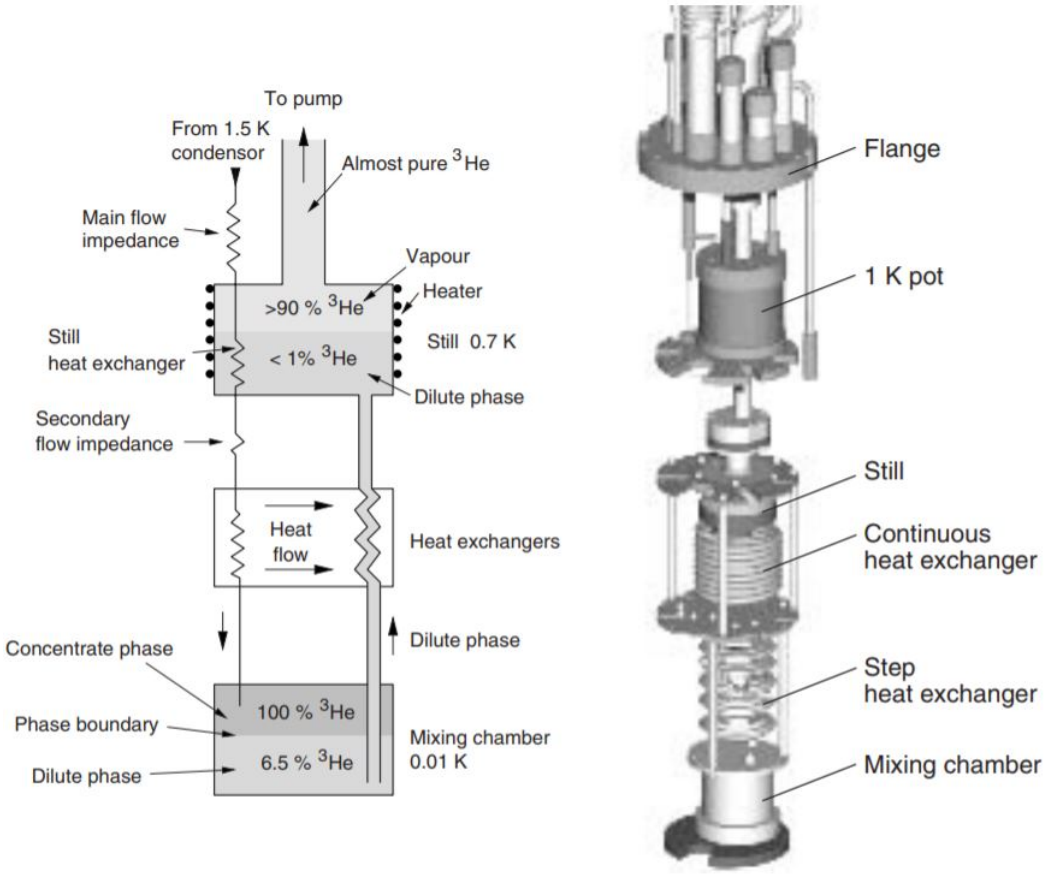

Figure 3-1: (a) Schematic representation of the inner ^{3}He/^{4}He circuit of a dilution refrigerator. (b) Design of the dilution unit of a commercial dilution refrigerator (see Ref. [23],[24]).

Once we have the two separated phases, one needs to remove the ^{3}He atoms from the diluted or ^{4}He-rich phase. Then, ^{3}He atoms from the pure phase will cross the boundary. The enthalpy difference between ^{3}He diluted in ^{4}He and in pure ^{3}He makes

the transition across the boundary an endothermic process that removes heat from the mixing chamber environment, cooling it. In the dilution fridge, this process takes place in the mixing chamber (see scheme in Fig. 3-1).

The question remains how to remove only ^{3}He atoms from the diluted phase. The way to achieve it is to introduce a distiller or 'still'. The 'still' contains some stationary ^{4}He alongside with a small portion of ^{3}He that comes from the mixing chamber. Due to the different vapour pressure between the two isotopes, ^{3}He gets distilled and leaves the mixing chamber. The still is heated sufficiently so that the temperature doesn't drop to a level where the vapor pressure is to low for the circulation to go on. As long as ^{3}He gets pumped out of the 'still', its concentration in the liquid phase of the distiller will decrease. As a result, an osmotic pressure between mixing chamber and 'still' appears, pulling ^{3}He atoms into the latter chamber.

The whole circuit for ^{3}He (and ^{4}He) atoms is depicted in Fig. 3-1 a). Apart from the mixing chamber and 'still', there is a heat exchanger and the $1K$ pot ($1.5K$ condensor). This scheme shows how the ^{3}He evaporated from the 'still' through pumping is brought to the $1K$ pot, where it is precooled (inbetween, ^{3}He usually flows through a nitrogen trap, where it is puriefied). The flow of ^{3}He condenses in the main flow impedance. Then, it goes through two counterflow heat exchangers, where it is further cooled down before entering the pure phase of the mixing chamber. Additionally, the ^{3}He in the ^{4}He-rich phase of the mixing chamber streams back to the 'still' due to the osmotic pressure, as discussed before. On its way to the distiller, ^{3}He flows through the heat exchangers again, where it absorbs energy from the ^{3}He that goes into the mixing chamber and cools it down. In our system, a base temperature of around $0.08K$ is achieved with this method.

For a more detailed explanation please refer to Ref. [23],[24],[25].

3.2 Basic characterization

Let us start doing a basic characterization of the sample with a twist angle of $\theta = 1.23°$. Fig. 3-2 a) shows the longitudinal resistance R_{xx} measured across the sample

as a function of the voltage applied to the top and bottom gate, V_{tg} and V_{bg}. As we had discussed in Chapter 2.2, this enables us to modify the carrier density and electric displacement field in the sample independently. A solid white line indicates the displacement field axis, while a pink line shows the carrier density axis. As we can see, the system is conductive at charge neutrality ($n = 0$) when no displacement field is applied. Similarly to what happens with bilayer graphene, the resistance increases significantly when increasing the displacement field. This indicates the opening of a band gap, as discussed in Sections 1.3.1 and 1.3.2. When doping the sample (changing its carrier density), we reach the superlattice gap for both electron- and hole-like doping (n_s and $-n_s$ respectively). This superlattice gap is present at zero displacement field and disappears when we increase D, an effect that can be seen better in Fig. 3-3 a). But more interestingly, an extra pair of insulating states appears at half the superlattice density $n_s/2$. These insulating states are only present in a finite range of displacement fields, so that they are electrically tunable. Besides, they are not obtained in the single particle picture. They are therefore correlated insulators. These states might have a Mott-like mechanism similar to the one reported in MAG, resulting from the Coulomb repulsion of electrons in the flat bands.

We can compare this observations with the band structures shown in Section 1.3.2, Fig. 1-7 b-d). There is a remarkable agreement between both:

- A band gap opens at charge neutrality when an electric displacement field is applied.
- The superlattice gap disappears with increasing displacement field as a result of bands merging.
- A correlated insulating state appears at half the superlattice density as a result of the bands getting flatter when displacement field is applied.
- At some point, increasing D also enlarges the bandwidth. As a result, the correlated insulator only survives in a finite range of displacement fields.

Fig. 3-2 b) shows the Hall resistance R_H for negative displacement fields and for

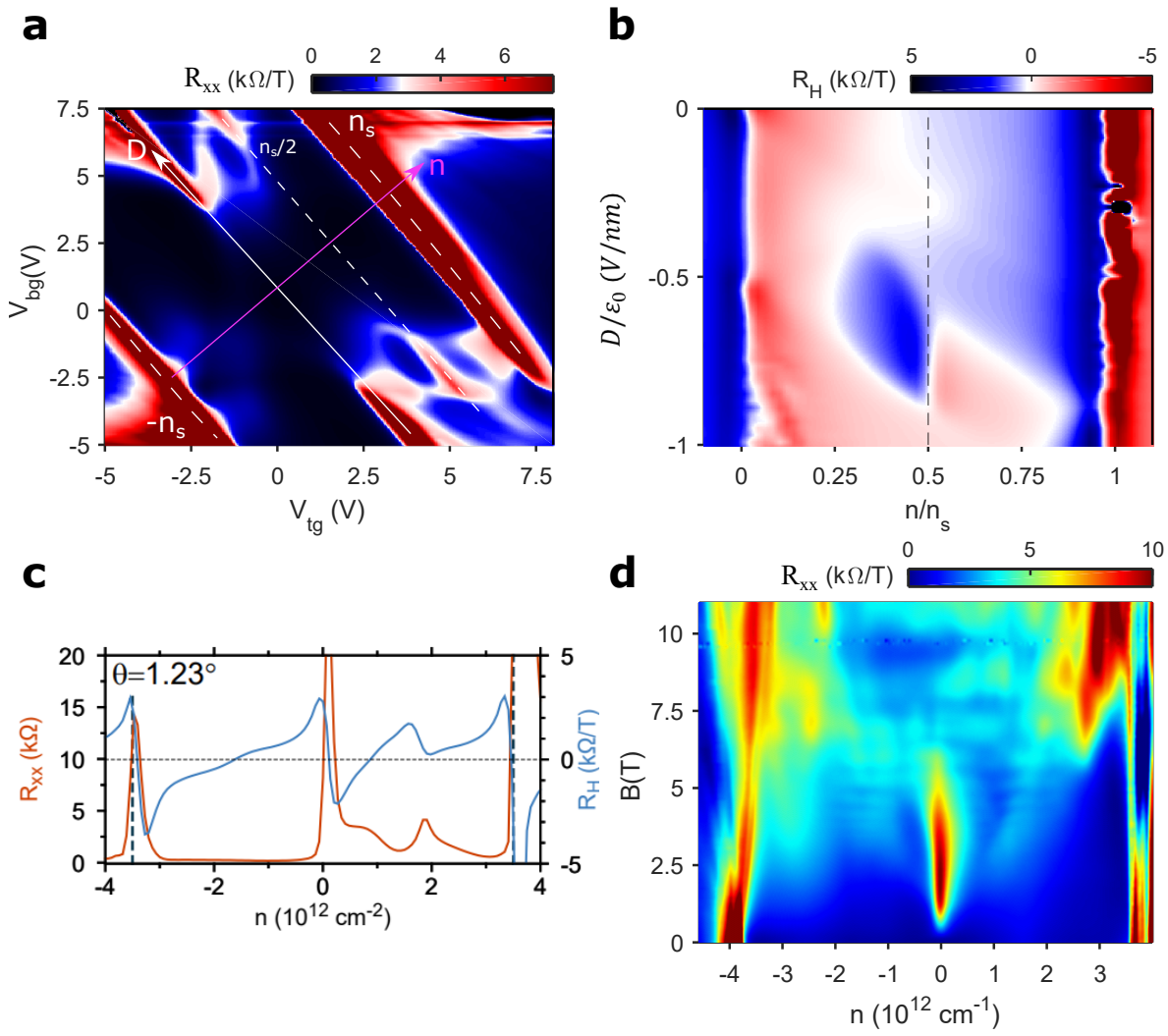

Figure 3-2: (a) Resistance for a TBBG sample with $\theta = 1.23°$ (the only one discussed in this work) as a function of top and bottom gate potentials, V_{tg} and V_{bg}. A solid white line denotes the displacement field axis. Also, white dashed lines mark the position of the superlattice density for both dopings and the presence of the correlated insulators at $n_s/2$. Additionally, the carrier density axis is marked with a pink solid line. (b) Map of the hall coefficient $R_H = \frac{d}{dB}(\frac{V_{xy}}{I})$ for negative displacement fields and positive carrier densities. The carrier density axis is normalized by the superlattice density. (c) Longitudinal resistance Rxx and hall coefficient R_H as a function of carrier density for a displacement field that exhibits the correlated insulating state at $n_s/2$. (d) Resistance versus carrier density and perpendicular magnetic field for a displacement field that only exhibits the gaps at charge neutrality and the superlattice density. All data are taken at $4K$.

carrier densities that range from $n/n_S = -0.1$ to $n/n_S = 1.1$. The Hall resistance is defined as $R_H = \frac{d}{dB}R_{xy} = \frac{d}{dB}(\frac{V_{xy}}{I})$. To compute it, we measure the transverse

resistance R_{xy} as a function of n and D for different perpendicular magnetic fields. Then, for each (n, D) point of the map, we fit R_{xy} versus B using a linear function. The sign of the Hall coefficient indicates the type of charge carriers in the system: positive R_H (blue region) indicates hole-like carriers, whereas negative R_H (red region) corresponds to electron-like carriers. As one would have expected, the carriers change from hole-like to electron-like when crossing both charge neutrality and the superlattice gap. At $n_s/2$, we also observe a sign change due to the fact that we have filled half of the band. But more interestingly, additional sign changes appear near $n_s/2$ for those displacements fields that exhibit the correlated insulating phase (between $D/\epsilon_0 \sim 0.4V/nm$ and $D/\epsilon_0 \sim 0.8V/nm$), indicating the creation of a many-body gap. The same behavior is observed for positive displacement fields, whereas no additional sign change appears for negative carrier densities due to the lack of the correlated insulator in that region. In Fig. 3-2 c) we plot the Hall coefficient R_H and the longitudinal resistance R_{xx} for just one value of D. Note that, apart from observing the same trends as the ones exposed in panel b), the sign changes at the gaps coincide with peaks in R_{xx}, as expected.

Finally, we measure the resistance R_{xx} as a function of carrier density and magnetic field for a displacement field that does not exhibit the correlated insulator at $n_s/2$ (Fig. 3-2 d). Accordingly, we only observe the insulating states at charge neutrality and $\pm n_s$. Interestingly, we can use this $n - B$ map to extract the superlattice density and the twist angle of the sample. The values obtained for this device are $n_s = 3.55 * 10^{12} cm^{-2}$ and $\theta = 1.23°$, respectively. Also, such a map enables us to find the capacitances c_{tg} and c_{bg} necessary to transform the $V_{tg} - V_{bg}$ map into an $n - D$ map with the right units. The procedure followed can be found in Appendix B.

All data presented in this section have been taken at a temperature of $4K$.

3.3 Temperature dependent data

We can now study the behavior of TBBG when the temperature of the system is modified. Fig. 3-3 a) shows a similar plot to the one in Fig. 3-2 a). The only

difference resides in the fact that the map has been rotated and the axis correspond now to carrier density and displacement field. The temperature of the system is now $70mK$, the base temperature of our dilution refrigerator. Apart from the features observed in Fig. 3-2 a) (gap opening at charge neutrality, superlattice band gaps closing at finite displacement field and the electrically tunable correlated insulators at $n_s/2$), an extra insulating state appears at one quarter the superlattice density $n_s/4$. Again, this insulating state does not appear in the single particle picture and is the result of correlations between electrons. Additionally, it is only present in a very small range of displacement fields.

If we take a cut at constant displacement field, we can measure the evolution of resistance with temperature and carrier density. The result is shown in Fig. 3-3 b). The depicted zone corresponds to the blue dashed line in panel a), which encompasses fillings from charge neutrality to the superlattice density and is located at $D/\epsilon_0 = -0.75V/nm$. As we can see, we have insulating states at $n = 0$ and $n = n_s$ that prevail until temperatures higher than $20K$. As for the correlated insulators at $n_s/2$ and $n_s/4$, they both disappear as we increase the temperature. The insulator at $n_s/4$ only persists until a temperature, of around $3K$, while the one at $n_s/2$ reaches higher temperatures of about $8K$. This difference is probably due to the different energy scales of the gaps associated with each insulator.

Similarly, we can do a cut at constant carrier density and show the resistance as a function of temperature and displacement field, as done in Fig. 3-3 b) for a density of $n_s/2$. This plot shows us the exact location of the insulating states and helps us determine the displacement field for with the resistance is enhanced $D_{opt}/\epsilon_0 = \pm 0.8V/nm$. Additionally, one can see how the peak resistance decreases in value (also visible in panel b)) and the insulating region broadens in displacement field when temperature is increased.

In panel d), we show several R-T traces for $D/\epsilon_0 = -0.75V/nm$ and densities that range from charge neutrality to half-filling (these traces are vertical cuts from the nT-map in panel b)). We can see three traces with clear insulating transitions:

- The black trace, which corresponds to charge neutrality (n=0).

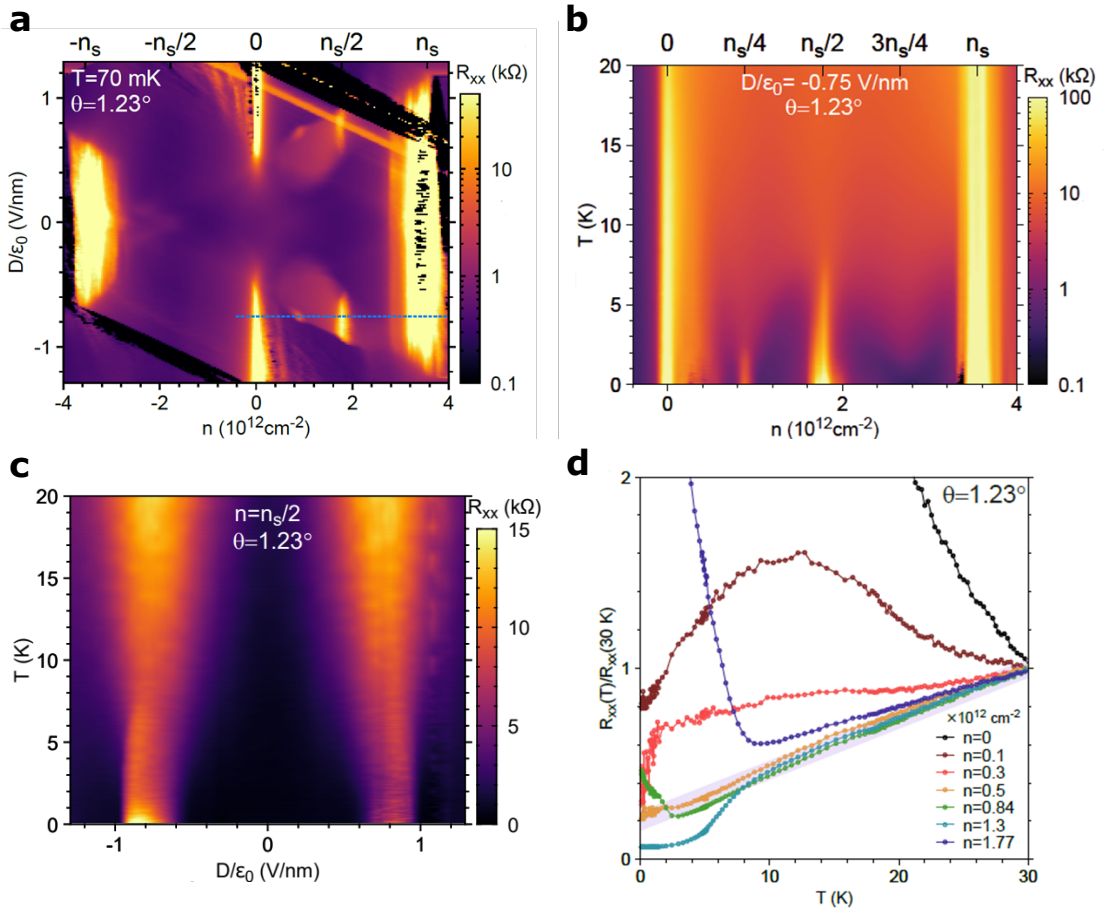

Figure 3-3: (a) Resistance as a function of carrier density and displacement field at the base temperature of our dilution refrigerator, $T = 70mK$. The blue dashed line corresponds to a displacement field $D/\epsilon_0 = -0.75nm^{-1}$. (b) Resistance as a function of carrier density and temperature for a fix displacement field of $D/\epsilon_0 = -0.75nm^{-1}$. (c) Resistance as a function of displacement field and temperature for half the superlattice density $n_s/2$. (d) Normalized resistance versus temperature for $D/\epsilon_0 = -0.75nm^{-1}$ and different carrier densities, ranging from charge neutrality ($n = 0$) to half-filling ($n = n_s/2 = 1.77 * 10^{12}cm^{-2}$).

- The dark blue trace, which corresponds to half the superlattice density ($n = n_s/2 = 1.77 * 10^{12}cm^{-2}$). The insulating transition starts at around $8K$.

- The green trace, which corresponds to one quarter the superlattice density ($n = n_s/4 = 0.84 * 10^{12}cm^{-2}$). The insulating transition starts at around $3K$.

It is interesting to note that the light blue R-T curve shows an abrupt decrease of resistance, which saturates at a finite value for low temperatures. This transition could indicate the proximity of our system to a superconducting transition similar

to the one that appears in MAG [4]. In fact, other groups have already observed a superconducting transition near the $n_s/2$ insulator for TBBG [15] [16].

Finally, one can see how the the resistance increases linearly with temperature for $T > 10K$. This is the case for densities ranging from $n = 0.5 * 10^{12} cm^{-2}$ to $n = 2.5 * 10^{12} cm^{-2}$, which are located away from charge neutrality. This T-linear behavior is similar to the strange metallic phase present in MAG [26] and discussed in Appendix A. As discussed in the supplementary information of Ref. [14], where this TBBG sample is also reported, the resistance shows no indications of linearity for the hole-doping region ($n < 0$). This behavior stays in accordance with the fact that no correlated physics are observed for those fillings. However, a more careful and thorough analysis of the existing data remains to be done before reaching any conclusions.

3.4 Magnetic field dependent data

In this section, we will exploit another parameter that can be tuned in the system: the external magnetic field applied to the TBBG sample. Some magnetic field dependent data were already shown in Fig. 3-2 d), although they were only used to determine the twist angle of the sample, as described in Section 3.2 and in Appendix B. Now, we aim to study the evolution of the correlated insulators with both perpendicular and in-plane magnetic fields.

3.4.1 Perpendicular magnetic field

Let us start studying how TBBG behaves when a magnetic field is applied perpendicular to the stack. Fig. 3-4 a) shows the same data as plotted in Fig. 3-3 a) but only for positive carrier densities (electron doping) and negative displacement fields. White dashed lines are plotted for all commensurate fillings ($\nu = 1, 2, 3$). As discussed before, we see band insulator states at $n = 0$ and $n = n_s$, while correlated states appear only at $n_s/4$ (adding one electron to the band, $\nu = 1$) and $n_s/2$ (adding two electrons, $\nu = 2$). This correlated states are encircled also by white dashed lines.

An extra blue dashed line at $D/\epsilon_0 = -0.75V/nm$ shows the displacement field at which both insulators appear.

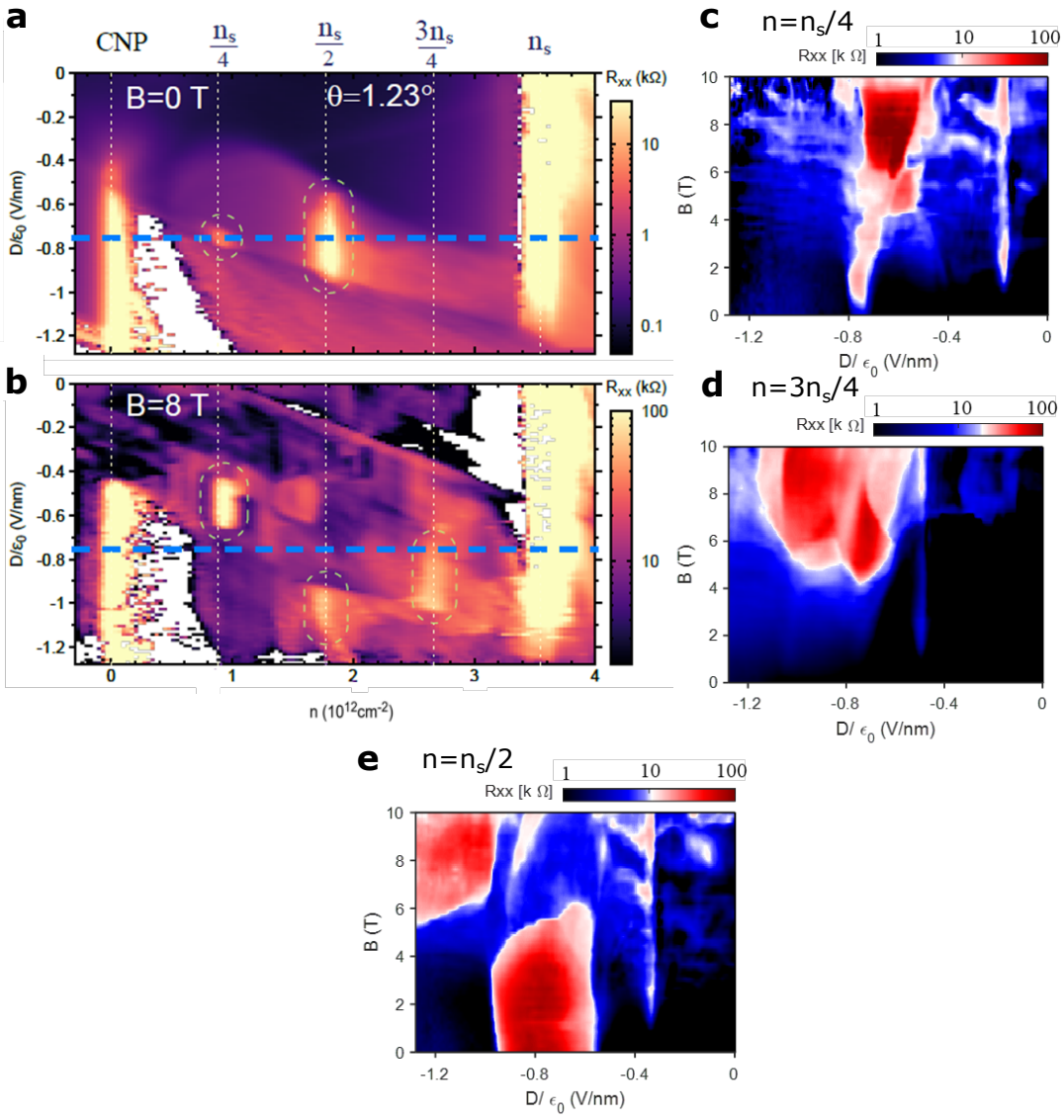

Figure 3-4: Perpendicular magnetic field response of TBBG. (a-b) Resistance as a function of carrier density and displacement field for perpendicular magnetic fields of $B = 0$ and $B = 8T$, respectively. Correlated insulators at integer electron fillings are circled. (c-e) Resistance at integer electron fillings as a function of displacement and perpendicular magnetic field. All data are taken at base temperature ($T = 70mK$).

Panel b) shows the $n - D$ resistance map for a perpendicular magnetic field of $B = 8T$. Several features can be observed:

- The correlated insulator at $n_S/2$ disappears at $D/\epsilon_0 = -0.75V/nm$ and arises

at a lower displacement field.

- The correlated insulator at $n_S/4$ vanishes at $D/\epsilon_0 = -0.75V/nm$ and appears at a higher displacement field.

- An extra correlated insulator appears at three quarters the superlattice density ($n = 3n_s/4$ or $\nu = 3$).

In conclusion, the system shows a correlated insulator at all commensurate fillings when applying perpendicular magnetic field, although the range of displacement fields at which they are present varies with $B_\perp$.

In order to keep track of this evolution, one can plot $D - B$ maps at all commensurate fillings. In other words, one can do a vertical cut at the $n - D$ map shown in panel b) and plot the corresponding displacement field trace as a function of magnetic field. The result is presented in Fig. 3-4 c-e). We can see how there seems to be a switching phenomenon at $B_\perp = 5T$. First, the correlated insulating state at $3n_s/4$ (panel d)) appears at around this magnetic field. The increase of resistance is monotonic for this insulator and no shift in displacement field is observed. In addition, we find signatures of a phase transition at $n_s/4$ (panel c)), resulting into a shift of the displacement field of the correlated insulator. Finally, the D-position of the correlated insulator at $n_s/2$ (panel e)) shifts abruptly at $B_\perp = 5T$, from $D/\epsilon_0 > -0.95V/nm$ to $D/\epsilon_0 < -0.95V/nm$. The origin of this strange behavior at $n_s/2$ is still unclear, but we can propose two plausible explanations: it is possible that the magnetic field induces a phase transition from a a valley-polarized metal to a spin-polarized insulator at low D as a result of competing spin and valley Zeeman effects, while the system transitions from a valley-polarized insulator to a metal at high D; alternatively, we could have mixed spin-valley polarized states at low perpendicular magnetic field that evolve into valley polarized states when increasing $B_\perp$.

It is worth pointing out that the physics discussed here do not only happen at negative displacement fields. An analogous behavior is found if studying the system at the same carrier densities for positive values of D.

3.4.2 In-plane magnetic field

In general, perpendicular magnetic field is not the best way to probe the physics of electronic spins, as it induces orbital effects. Alternatively, one can apply a magnetic field in the plane defined by the 2D stack, providing a more reliable way to study Zeeman effects.

Fig. 3-5 a) shows an $n - D$ map at a finite in-plane magnetic field of $B_{\parallel} = 8T$. We observe a markedly different behavior from the one exhibited by the system under $B_{\perp}$. The correlated insulating states at $n_s/4$ and $n_s/2$ do not shift in displacement field and remain at around $D/\epsilon_0 = -0.75V/nm$. Also, the correlated insulator at $3n_s/4$ appears at a similar D-position. Again, we can better analyze this trend by plotting the $D - B$ maps at commensurate fillings (Fig. 3-5 b-d)). For the three correlated insulators, the resistance increases smoothly with in-plane magnetic field. Additionally, the range of displacement fields over which the insulating states are present also increases with $B_{\parallel}$. This tendency is also illustrated in panel e), an $n - B$ map at $D/\epsilon_0 = -0.75V/nm$ (blue dashed line in panel a)). Note that this behavior is completely different from the one observed in MAG, where the correlated insulator at $n_s/2$ vanishes when in-plane magnetic field is applied [4] (see discussion in Section 1.2).

In order to draw some conclusions about the nature of the insulating states, we can analyze how the sizes of the correlated gaps evolve with $B_{\parallel}$. In Fig. 3-5 f), we plot the resistance of the correlated gap at $n_s/2$ as a function of T^{-1} for different magnetic fields. Following the general procedure used in transport measurements, we fit the resistance with an Arrenhius law $R_{xx} \sim e^{-\Delta/2kT}$, where Δ represents the size of the gap and k stands for the Boltzmann constant (see solid lines in the main plot). The purple dots in the inset of Fig. 3-5 f) show the values of the gap obtained for each magnetic field.

We can then express the gap size as $\Delta = g\mu_B B_{\parallel}$. A linear fit results into a g-factor of $g_{n_s/2} = 0.52$. Other studies in TBBG have reported a g-factor of 2 [15] [16], which corresponds to the Zeeman effect. They therefore attribute this behavior to a purely

spin-polarized ground state for the correlated insulator at half-filling. In their picture, a gap opens at $n_s/2$ due to the correlations between electrons. Spins align in each of the resulting bands (spin-up for the upper band and spin-down for the lower). As a result, the application of the magnetic field shifts the central energy of the bands and enlarges the gap by a factor of $g = 2$. However, this is clearly not the case in our system, as the g-factor we obtain is much smaller than 2. The discrepancy could be due to disorder in the sample. Alternatively, we could have a mixed spin and valley polarization of the ground state, which would account for the reduced g-factor compared to a pure spin-polarized state.

Finally, the inset of Fig. 3-5 f) also shows the gap sizes for the correlated insulators at $n_s/4$ and $3n_s/4$. We obtain $g = 0.09$ for both insulating states. Please refer to Ref. [14] for further analysis.

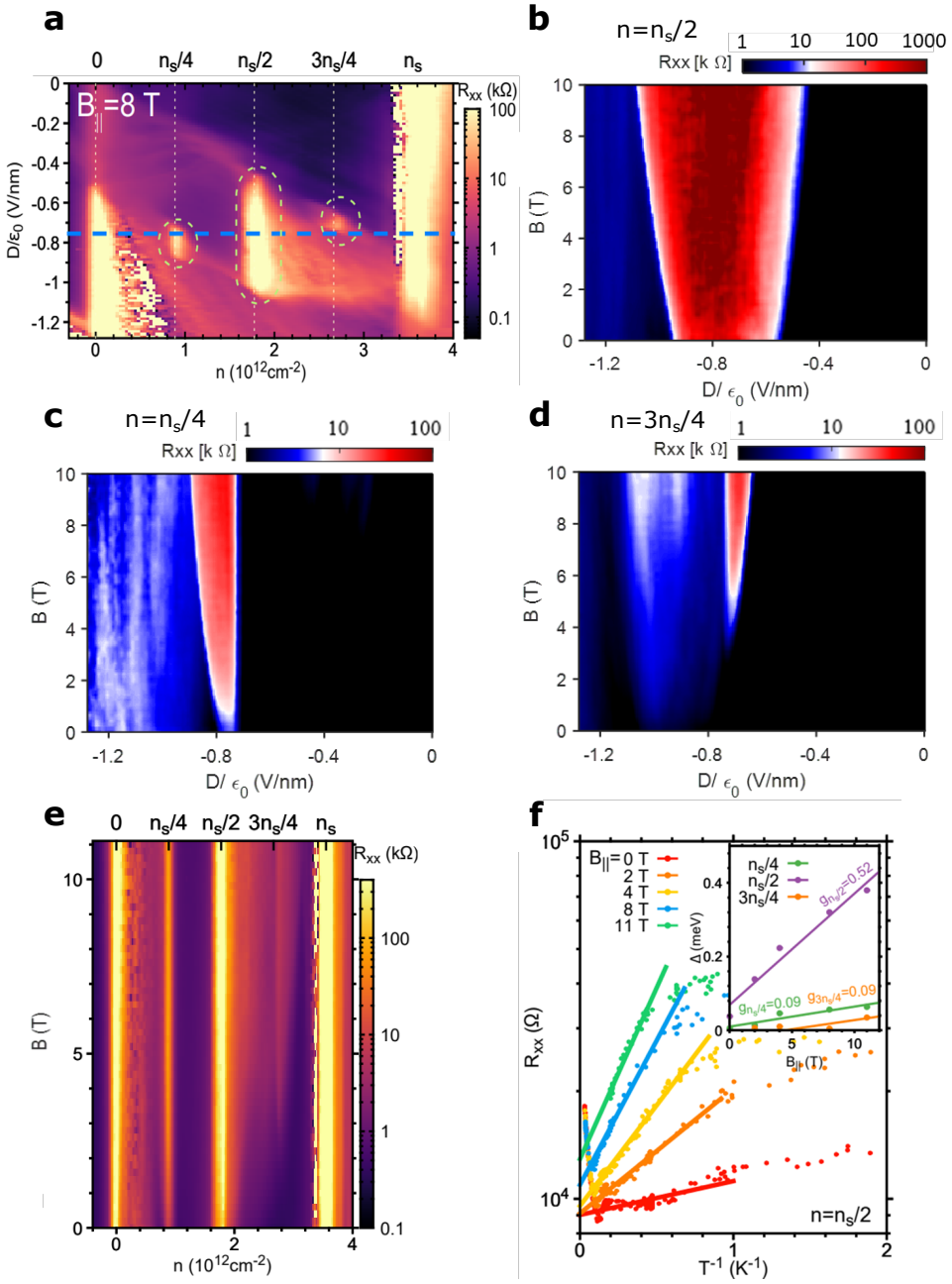

Figure 3-5: In-plane magnetic field response of TBBG. (a) Resistance as a function of carrier density and displacement field for a parallel magnetic field of $B = 8T$. Correlated insulators at integer electron fillings are circled. (b-d) Resistance at integer electron fillings as a function of displacement and parallel magnetic field. (e) Response to in-plane magnetic field at the displacement field $D/\epsilon_0 = -0.75nm^{-1}$ marked by the blue dashed line in panel (a). (f) Resistance of correlated insulator at $n_s/2$ at the displacement field $D/\epsilon_0 = -0.75nm^{-1}$ for different parallel magnetic fields. The solid lines are fits using an Arrenhius law $\sim e^{-\Delta/2kT}$. The inset shows the gap sizes for all three integer fillings obtained from the fittings. The g-factors obtained are 0.52 for $n_s/2$ and 0.09 for $n_s/4$ and $3n_s/4$. All data are taken at base temperature ($T = 70mK$).

Chapter 4

Conclusion

In this work, we have extended the study of strongly correlated physics to Moiré systems different than magic angle graphene. In particular, we propose a new platform based on two rotated sheets of Bernal-stacked bilayer graphene, which we referred to as twisted bilayer-bilayer graphene or TBBG.

Several TBBG samples were fabricated. The fabrication procedure is extensively described in Chapter 2. First, we introduce the 'tear and stack' technique, used to stack the two sheets of bilayer graphene together rotated by the desired twist angle. Then, we review the different steps necessary to define the shape of the device and to evaporate the contacts and gates.

All fabricated samples were measured in a dilution refrigerator. However, we only report on one of them here. We study the behavior of this sample, which has a twist angle of $\theta = 1.23°$, when electric displacement fields and perpendicular and in-plane magnetic fields are applied, as a well as when temperature is modified. The following results are obtained:

- A band gap opens at charge neutrality when displacement field is applied, similarly to what happens in AB bilayer graphene. On the other hand, the superlattice gap decreases with D until it eventually disappears.

- Correlated insulating states appear at all integer fillings of the Moiré unit cell and are only present in a finite range of displacement fields. The insulator at

$3n_s/4$ only emerges when a magnetic field is applied.

- The correlated insulators disappear with increasing temperature. T-linear traces can be observed for certain fillings near $n_s/2$.

- When perpendicular magnetic field is applied, the correlated insulators undergo phase transitions that are characterized by shifts in displacement field.

- Under parallel magnetic field, the resistance in all correlated insulators increases and the range of displacement fields exhibiting insulating behavior broadens. An analysis of the gap size reveals a g-factor of 0.52 for $n_s/2$ and 0.09 for $n_s/4$ and $3n_s/4$.

These observations match with the theoretical predictions exposed in Section 1.3.2. On the one hand, the schematic representation in Fig. 1-7 e-g) captures the fact that flat bands and therefore correlated physics only appear in a finite range of displacement fields. The numerical computation of the band structure, shown in Fig. 1-7 b-d), confirms this behavior. In addition, the band opening at charge neutrality and the closing of the superlattice gap are also captured in the simulations.

Finally, we study magic angle graphene, another Moiré system, in Appendix A and identify a strange metallic phase for fillings near the correlated insulator at $n_s/2$. This phase is characterized by a T-linear resistivity above a certain coherence temperature. Besides, a transport 'scattering rate' that satisfied a universal Planckian form is obtained for the system.

The work on TBBG and MAG exposed in this thesis has resulted in two publications, Ref. [14] and [26].

Appendix A

Strange metal behavior in magic angle graphene with near Planckian dissipation

Magic angle graphene (MAG) has been thoroughly studied since its discovery on April 2018 and its phase diagram has evolved very rapidly. One of the new phases that has been discovered in this strongly correlated system is a region of T-linear resistivity above a small, density dependent crossover temperature. A more detailed study about these phenomenon can be found in [26].

A big number of strongly correlated materials exhibit properties that differ from the expected Fermi liquid (FL) behavior. Some families of materials (e.g. ruthenates [27]) show a non-Fermi liquid (NFL) behaviour in an intermediate range of temperatures, with a transition to FL below a coherence temperature T_c. Other materials, such as cuprates [28], show the NFL behavior until $T \to 0$. This phases are marked by a lack of coherent quasiparticle excitations and are characterized, among others properties, by a T-linear resistivity profile $\rho(T) \sim T$.

We hereby study the transport properties of the metallic states in MAG as a function of temperature for a wide range of fillings. Fig. A-1b) shows two different resistivity traces. The red one is taken at a filling $\nu = -2 - \delta$ (half-filling for hole doping and adding extra holes; see Fig. A-1a)) and the pink one at $\nu = 2 - \delta$

(half-filling for electron doping and adding extra holes). Both of them show a linear behaviour that starts at a value of T_{coh} around $7K$ for the former and $0.5K$ for the latter and lasts until (at least) $30K$. From a linear fit for $T > T_{coh}$ one can obtain a slope of $d\rho/dT \approx 335\Omega/K$ and $d\rho/dT \approx 95\Omega/K$, respectively. Six different samples were analyzed and the slopes where mostly contained within these two values. However, no trend with respect to twist angle could be observed.

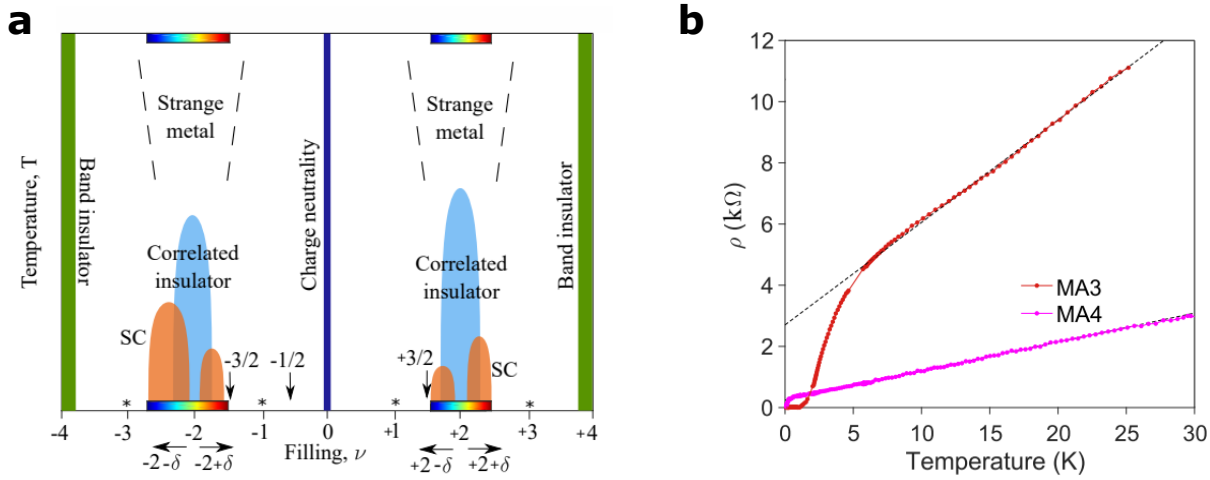

Figure A-1: (a) Schematic phase diagram of MAG as a function of filling ν. The strange metal behaviour is mostly found in the regions where strongly correlated phenomena appear. The orange domes represent the superconducting domes, while the blue ones stand for the correlated insulators at half the supperlattice density. (b) Resistivity ρ as a function of temperature for device MA3 ($\theta = 1.02°$) at $\nu = -2 - \delta$ and for device MA4 ($\theta = 1.16°$) at $\nu = 2 - \delta$, showing a T-linear behavior until $30K$.

We can plot the resistance as a function of temperature for different fillings, as shown in Fig. A-2. In panel (a) we are showing the density range marked in Fig. A-1a) on the hole-doped side, while panel (b) shows the density range on the electron-doped site denoted also in Fig. A-1a). At low temperatures, the behavior is complex and depends highly on the speciffic filling. However, above a certain temperature T_{coh}, which varies with filling, all traces look qualitatively similar and show a monotonic trend, being also reasonably parallel. Please note that these traces are taken at fillings where strongly correlated phenomena are present.

One can also check what happens at other fillings (see Fig. A-2c-d)). Panel c) shows that there is no clear indication of linear resistivity at charge neutrality and

at slightly lower fillings ($\nu \sim -1/2$). Panel d) shows how there is no sign of linear behavior for $\nu \sim -3/2$, while there are some signatures for $\nu \sim 3/2$. Thus, one can conclude that T-linear resistivity is confined to regions near $\nu = -2$ and $\nu = 2$, in other words, around the correlated insulators of the system.

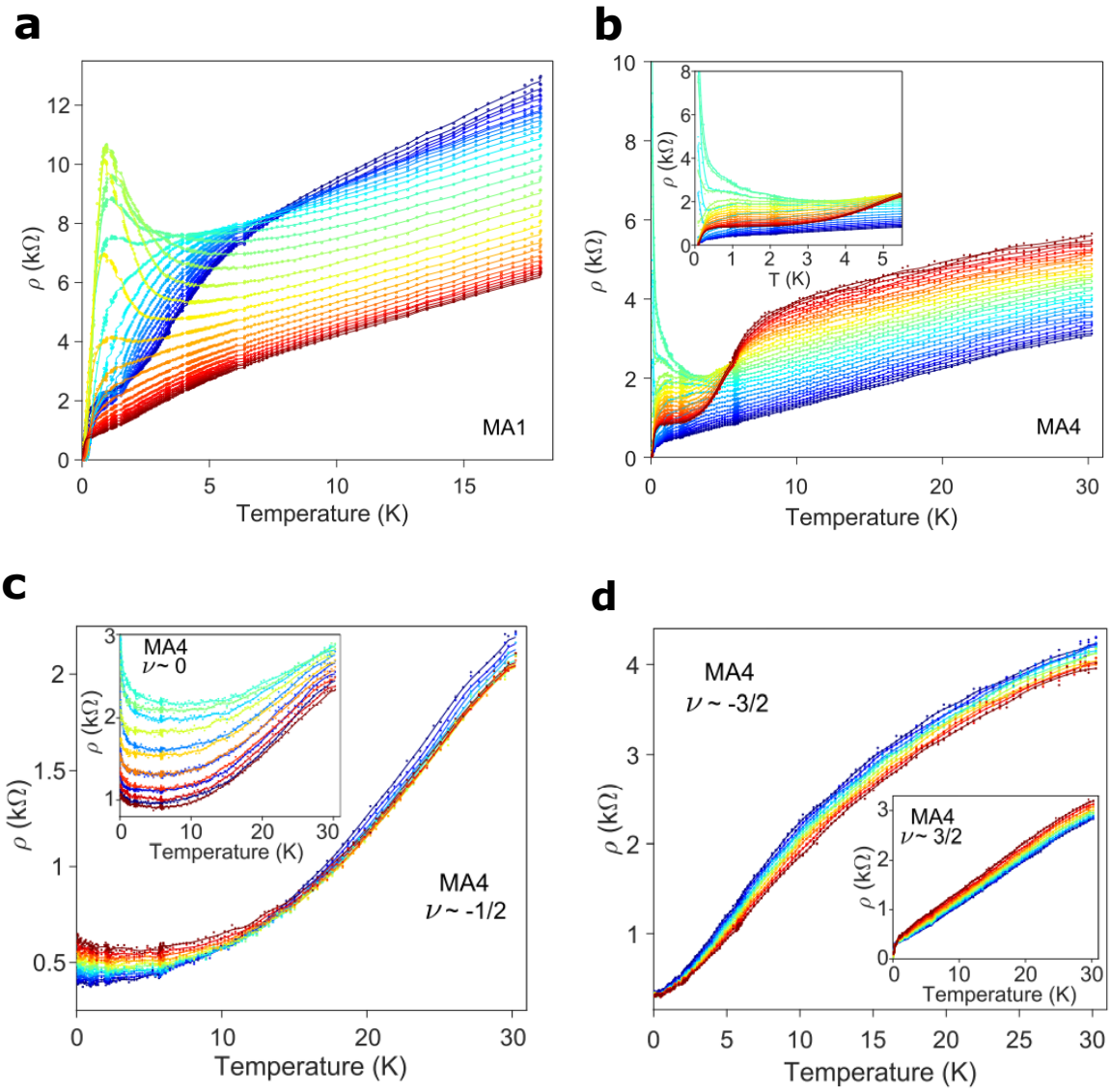

Figure A-2: (a) Resistivity as a function of temperature for MA1 ($\theta = 1.16°$) around filling $\nu = -2$ (see colorbar in Fig. A-1a). (b) Resistivity as a function of temperature for MA4 ($\theta = 1.16°$) around $\nu = 2$ (see colorbar in Fig. A-1a). (c) and (d) show resistivity traces as a function of temperature for MA4 at different fillings, indicated in each panel.

We can compare the values of resistance and slope in MAG to the ones of one of

the most well studied examples of strange metallic behavior: cuprates near optimal doping for the hole-doped region. If one takes the transport values of resistivity and normalizes them by the interplane distance (to account for the fact that cuprates are 3D system while MAG is a 2D material), one obtains values of resistivity that lie in the same order of magnitude. As for the slope, cuprates show values around $23\Omega/K$, slightly smaller than in MAG.

One can do a more accurate analysis of the slope to study to what extent it varies with filling factor. To do so, we plot in Fig. A-3a) the resistivity of the sample MA2 ($\theta = 1.05°$) near $\nu = -2$ for a few fillings (note that the correlated insulator at $\nu = -2$ corresponds to a carrier density of $-1.3 * 10^{12} cm^{-2}$). By fitting straight lines for temperatures bigger than $T_{coh} = 8K$, we can obtain the slope $d\rho/dT$ in this density range. Fig. A-3b) shows how the slope varies non-monotonically with carrier density.

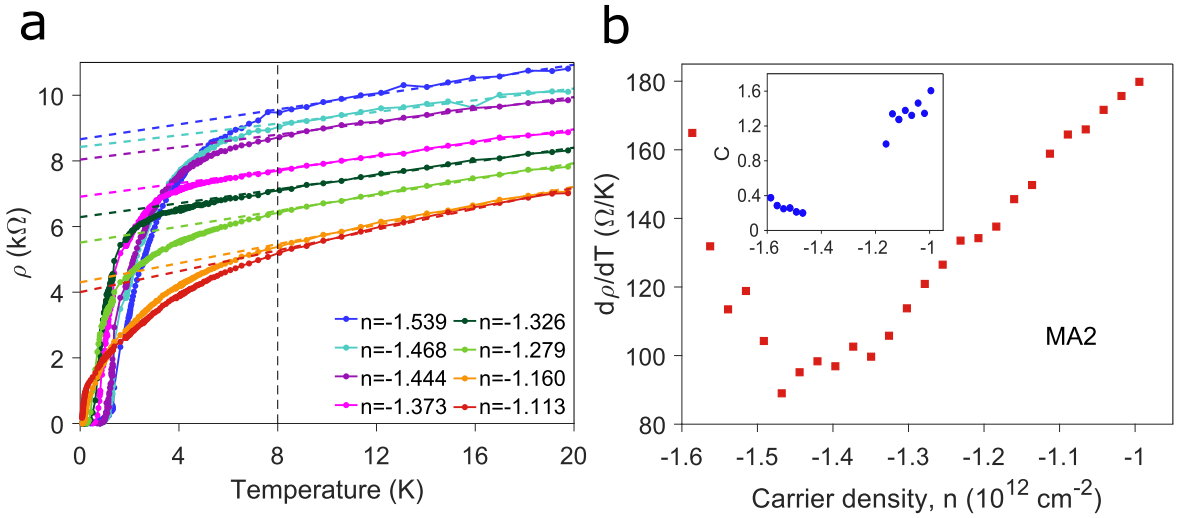

Figure A-3: (a) Resistivity traces as a function of temperature for different fillings around the correlated insulator at $\nu = -2$ for MA2 ($\theta = 1.05°$). For this sample, the correlated insulating state corresponds to a carrier density of $-1.3 * 10^{12} cm^{-2}$. Linear fits are done above $T_{coh} \sim 8K$. (b) Slope of resistivity ($d\rho/dT$) as a function of filling for $T > 8K$ obtained using a linear fit. The inset shows the prefactor C of the scattering rate Γ for fillings where SdH oscillation data are available.

For the moment we have just discussed that MAG shows T-linear resistivity

around fillings where strong interactions are present in the system, a behavior that is also present in other strongly correlated materials characterized by the lack of coherent quasiparticle excitations. Additionally, it has been proposed that such materials have a scattering rate Γ that is determined by a universal Planckian bound. In order to obtain the scattering rate from the resistivity we can use the procedure first introduced in Ref. [29]. One can write the scattering rate as $\Gamma = Ck_BT/\hbar$ and define the prefactor C as

$$C = \frac{\hbar}{k_B}\frac{e^2 n_c(0)}{m^*(0)}\frac{d\rho}{dT}$$

where $m*(0)$ and $n_c(0)$ are the effective mass and density for $T \to 0$. This formula can be derived by assuming that the resistivity of the system can be described by a Drude-like expression.

We already have the values of the slope for sample MA2 (see Fig. A-3b)). As for the effective density and mass values, they can be obtained from the Shubnikov-de Hass (SdH) quantum oscillation data published for this same device in Ref. [4] (see also Section 1.2). Note also that the effective density is not the carrier density we induce with the gates. For example, for fillings around $\nu = -2 - \delta$, it corresponds to the carrier density induced by the gates with respect to the correlated insulator at $\nu = -2$ instead of charge neutrality [4]. The coeficient C obtained for sample MA2 is shown in the inset of Fig. A-3b). Around the correlated insulator, Γ varies from around 0.2-0.4 when adding a few holes (with respect to the insulating state) and from 1.0-1.6 when adding a few electrons. We do not have values around $-1.3*10^{12}cm^{-2}$, in other words at the correlated insulator, because SdH oscillations could not be obtained in that region. However, we can conclude that the prefactor C of the scattering rate Γ is of the order of 1.

We can compare this value with the ones computed for other strongly correlated materials. Interestingly, they also show $C \sim 1$. For example, cuprates show coefficients ranging from $C \sim 0.7 - 1.2$ on both sides of the phase diagram. A more detailed list containing such materials is presented in Ref. [26].

The mechanism that generates this behavior is still unknown, although some the-

oretical proposals are already appearing (see Ref. [26] for a more general discussion of the possible mechanisms). A satisfactory theory, however, must be able to explain the following charactersistics observed in our samples:

1. T-linear resistivity around $\nu = \pm 2$ with near Planckian scattering rates.

2. Weak dependency of the resistivity slope $d\rho/dT$ as a function of filling or carrier density.

3. Existence of a coherence temperature T_{coh} above which transport is unconventional (T-linear).

4. Low sensitivity of the resistivity to the Fermi temperature T_F (in other correlated materials, the T-linear regime disappears before reaching T_F; for MAG, however, linear behavior prevails at higher temperatures than the T_F of the system, which is around $30K$)

Appendix B

Obtaining of superlattice density, twist angle and $n - D$ parameters

In this appendix, we will discuss how to obtain the value of the superlattice density and the twist angle of a sample, as well as the parameters of the transformation from gate voltages to density and displacement field

$$n = [c_{tg}(V_{tg} - V_{tg,0}) + c_{bg}(V_{bg} - V_{bg,0})]/e \tag{B.1}$$

$$D = [-c_{tg}(V_{tg} - V_{tg,0}) + c_{bg}(V_{bg} - V_{bg,0})] \tag{B.2}$$

which was already defined in Chapter 2. c_{tg} and c_{bg} are the top and bottom gate voltage, respectively. $V_{tg,0}$ and $V_{bg,0}$ account for the offset and e is the elementary charge.

To obtain all these values, we start taking a look at a $V_{tg} - V_{bg}$ map, as the one shown in Fig. 3-2 a). As we can see, all features (e.g. insulating states) are rotated in this map. The angle of this rotation is determined by the top and bottom gate capacitances. We can rotate the map, so that all correlated insulator appear vertical. By doing this, we will express the carrier density as

$$\tilde{n} = aV_{tg} + bV_{bg}. \tag{B.3}$$

In other words, we can define c_{tg} and c_{bg} up to a common factor f ($c_{tg} = f * a$ and $c_{bg} = f * b$). This factor accounts for the fact that the density units of $\tilde{n}$ are arbitrary (the displacement field units of the rotated map will be arbitrary too). Nonetheless, we can now measure $\tilde{n} - \tilde{D}$ maps that have the same orientation as regular $n - D$ ones.

To obtain the superlattice density, the twist angle and the factor f, we have to take an $n - B$ map and fit the Landau levels that appear. Both in MAG and TBBG superlattices, the Landau levels take the form [4]

$$\frac{n}{n_s} = N\frac{\Phi}{\Phi_0} + s \tag{B.4}$$

where $\Phi = B_\perp * A$ is the magnetic flux that penetrates each unit cell of area A, $\Phi_0 = h/e$ is a flux quantum, N is the Landau level index ($N = \pm 1, \pm 2, \pm 3, ...$) and s determines which fan we are considering ($s = 0$ for $n = 0$, $s = 1$ for $\pm n_s$ etc.). This equation is obtained from the Wannier diagram [30], which describes the Hofstadter's butterfly model [31]. Let us particularize the levels for the gap at charge neutrality. In this case, we have $\frac{n}{n_s} = N\frac{B_\perp A}{\Phi_0}$, which reads as $n = \frac{B}{\Phi_0} n_s N A$. But we also now that there are four electrons per Moiré unit cell at the superlattice density, resulting in $n_s = 4/A$. Thus, we can rewrite the Landau levels for this gap as $n = \frac{B}{\Phi_0} q$, where $q = \pm 4, \pm 8, \pm 12, ...$ are called the filling factors. The red lines in Fig. B-1 illustrate the positions of these Landau levels. They correspond to resistance minima that emanate from a certain density at zero magnetic field, which corresponds in this case to $n = 0$. The density of the Landau levels varies with B according to the previous equation. Each set of Landau levels is commonly referred to as Landau fan because of its characteristic shape.

Let us find now the value of the factor f. From equation B.3, it follows that $n = f * \tilde{n} + \tilde{n}_0$, where $\tilde{n}_0$ stands for the offset density in our arbitrary units (we have to account for it now as we did not introduce the offset in gate voltages when defining $\tilde{n}$). First, we correct the offset in carrier density. Then, we should notice that we can shrink or enlarge the density axis by changing the value of f. In other words, we can

modify the slope of the red fan computed using equation B.4 (which does not depend on unknown parameters) with respect to the features of the 2d map. Thus, we need to tune f until the computed red fan matches the resistance minima of the map, a condition that will determine the factor f. As we discussed before, this also defines the capacitances c_{tg} and c_{bg} and, consequently, the $n - D$ transformation.

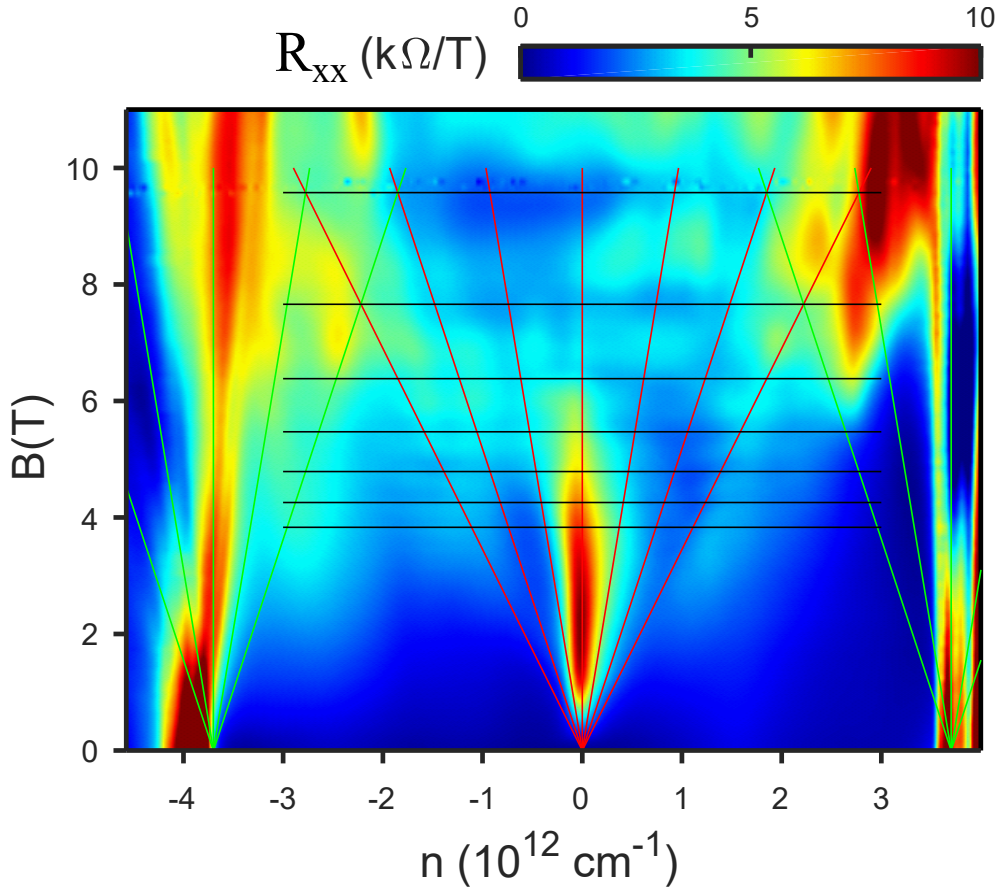

Figure B-1: Resistance as a function of carrier density and perpendicular magnetic field for a TBBG sample with $\theta = 1.23°$. The displacement field is chosen so that only the insulating states at $n = 0$ and $n = \pm n_s$ are present. The red Landau fan shows the Landau levels for the insulator at $n = 0$, whereas the green ones indicate the Landau levels of the superlattice band insulators. The black horizontal lines show the crossings between Landau levels. The $n - B$ map has been taken at $4K$.

The question remains how to find the superlattice density and the twist angle. The former is straightforward to find. There are also Landau fans that emanate from the superlattice gap (or the correlated insulators at integer fillings, depending on the displacement field chosen). The scaling of the density axis done when tuning f will

have already defined the position of these extra fans (plotted in green in Fig. B-1). One can just read the density at which the different Landau levels cross at zero magnetic field, which will correspond to the superlattice density n_s (or $n_s/2$ if we where considering the insulating state at half-filling).

In addition, it can be proven that the superlattice density n_s is related to the twist angle of MAG or TBBG by [4]

$$n_s = \frac{4}{A} \approx \frac{8\Theta^2}{\sqrt{3}a^2} \tag{B.5}$$

where A is the area of the Moiré unit cell and $a = 0.246nm$ is the lattice constant of graphene. The first equality just corresponds to the definition of n_s as the density for which we fill each set of superlattice bands. In other words, the situation in which each Moiré unit cell contains four electrons. The second equality involves an approximation that relates the area of the unit cell to the twist angle. Thus, we can compute θ easily once we know n_s.

There is a second way to estimate the superlattice density and, consequently, the twist angle. It relies on the fact that adjacent Landau fans intersect when $\frac{\Phi}{\Phi_0} = \frac{1}{p}$, where p is an integer [4]. This condition can be derived from equation B.4. Substituting $\Phi = B_\perp A$, one obtains

$$\frac{1}{B} = \frac{pA}{\Phi_0}. \tag{B.6}$$

Thus, Landau level crossings are expected at periodic intervals of $1/B$. The periodicity will define the area of the Moiré unit cell and therefore also n_s and θ. The black horizontal lines in Fig. B-1 show the magnetic fields that present these crossings. To better visualize the crossings, one could also plot the resistance as a function density and the inverse of magnetic field. In that case, the crossings would appear equidistant in the $1/B$ axis.

For the TBBG sample studied in this work, we obtain the following values: $\theta = 1.23°$, $n_s = 3.55 * 10^{12} cm^{-2}$, $c_{tg} = 1.06 * 10^{-3} Fm^{-2}$, $c_{bg} = 7.14 * 10^{-4} Fm^{-2}$, $V_{tg,0} = 0.41V$ and $V_{bg,0} = -0.04V$.

Bibliography

[1] A. K. Geim & I. V. Grigorieva, Van der Waals heterostructures. *Nature* **499**, 419-425 (2013).

[2] K. S. Novoselov, A. Mishchenko, A. Carvalho, A. H. Castro Neto, 2D materials and van der Waals heterostructures. *Science* **353** (2016).

[3] Cao, Y., Fatemi, V., Demir, A., Fang, S., Tomarken, S. L., Luo, J. Y., Sanchez-Yamagishi, J. D., Watanabe, K., Taniguchi, T., Kaxiras, E. , Ashoori, R. & Jarillo-Herrero, P. Correlated Insulator Behaviour at Half-Filling in Magic Angle Graphene Superlattice. *Nature* **556**, 80-84 (2018).

[4] Cao, Y., Fatemi, V., Fang, S., Watanabe, K., Taniguchi, T., Kaxiras, E. & Jarillo-Herrero, P. Unconventional superconductivity in magic-angle graphene superlattices. *Nature* **556**, 43-50 (2018).

[5] Bistritzer, R. & MacDonald, A. H. Moiré bands in twisted double-layer graphene. *Proc. Natl. Acad. Sci. U. S. A.* **108**(30), 12233-12237 (2011).

[6] J. L. Santos, N. Peres and A. C. Neto, Graphene Bilayer with a Twist: Electronic Structure. *Phys. Rev. Lett.* **99**, 256802 (2007).

[7] Eslam Khalaf, *et al.*, Magic angle hierarchy in twisted graphene multilayers. arXiv:1901.10485 (2019)

[8] Aaron Sharpe, *et al.*, Emergent ferromagnetism near three-quarters filling in twisted bilayer graphene. arXiv:1901.03520 (2019)

[9] Y. Cao, *et al.*, Twisted Graphene Superlattices: Superconductivity, Electron Correlations and Beyond. APS Meeting Abstracts (2019)

[10] Xiaobo Lu, *et al.*, Superconductors, Orbital Magnets, and Correlated States in Magic Angle Bilayer Graphene. arXiv:1903.06513 (2019)

[11] M. Yankowitz, *et al.*, Tuning superconductivity in twisted bilayer graphene. *Science* p. eaav1910 (2019)

[12] Guorui Chen, *et al.*, .Nature Physics (2019)

[13] Philip Kim, KITP: Correlations in Moire Flat Bands (Jan 14-25, 2018)

[14] Yuan Cao, Daniel Rodan-Legrain, Oriol Rubies-Bigorda, Jeong Min Park, Kenji Watanabe, Takashi Taniguchi and Pablo Jarillo-Herrero, Electric Field Tunable Correlated States and Magnetic Phase Transitions in Twisted Bilayer-Bilayer Graphene. arXiv:1903.08596

[15] X. Liu, *et al.*, Spin-polarized Correlated Insulator and Superconductor in Twisted Double Bilayer Graphene. arXiv:1903.08130

[16] Cheng Shen, *et al.*, Observation of superconductivity with Tc onset at 12K in electrically tunable twisted double bilayer graphene. arXiv:1903.06952

[17] Thiti Taychatanapat and Pablo Jarillo-Herrero, Electronic Transport in Dual-Gated Bilayer Graphene at Large Displacement Fields. *Phys Rev. Lett.* **105**, 166601 (2010)

[18] Jong Yeon Lee, *et al.*, Theory of correlated insulating behaviour and spin-triplet superconductivity in twisted double bilayer graphene. arXiv:1903.08685

[19] Kim, K.*et al.* Van der Waals Heterostructures with High Accuracy Rotational Alignment. *Nano Lett.* **16**, 1989 (2016).

[20] K. Kim, *et al.* Tunable moiré bands and strong correlations in small-twist-angle bilayer graphene. *Proc. Natl. Acad. Sci. U. S. A.* **114**(13), 3364-3369 (2017).

[21] Cao, Y. *et al.* Superlattice-induced insulating states and valley-protected orbits in twisted bilayer graphene. *Phys. Rev. Lett.* **117,** 116804 (2016)

[22] L. Wang *et al.* One-dimensional electrical contact to a two-dimensional material. *Science* **342** 614 (2013).

[23] Christian Enss and Siegfried Hunklinger, Low-Temperature Physics, (Springer, Heidelberg, 2005)

[24] F. Pobell, Matter and Methods at Low Temperatures, (Springer, Heidelberg 1996)

[25] Oxford Instruments (http://www.oxford-instruments.cn/OxfordInstruments/media/nanoscience/Priciples-of-dilution-refrigeration_v14.pdf)

[26] Yuan Cao, Debanjan Chowdhury, Daniel Rodan-Legrain, Oriol Rubies-Bigorda, Kenji Watanabe, Takashi Taniguchi, T. Senthil, Pablo Jarillo-Herrero. Strange metal in magic-angle graphene with near Planckian dissipation, arXiv:1901.03710

[27] N. E. Hussey *et al.* Normal-state magnetoresistance of sr2ruo4. *Phys. Rev.B* **57**, 5505 (1998).

[28] P. Giraldo-Gallo *et al.* Scale-invariant magnetoresistance in a cuprate superconductor. *Science* **361**, 479 (2018).

[29] J. A. N. Bruin *et al.* Similarity of scattering rates in metals showing t-linear resistivity. *Science* **339**, 804 (2013).

[30] Wannier, G.H., A result not dependent on rotationality for Bloch electrons in a magnetic field. *Phys. Status Solidi b* **88,** 757-765 (1978)

[31] Hofstadter, D.R., Energy levels and wave functions of Bloch electrons in rational and irrational magnetic fields. *Phys. Rev. B* **14,** 2239-2249 (1976)